Nonlinear Processes in Geophysics (2003) 10: 151–177

Nonlinear Processes in Geophysics

Geometric aspects of HF driven Langmuir turbulence in the ionosphere

E. Mjølhus[1], **E. Helmersen**[2], **and D. F. DuBois**[3]

[1]University of Tromsø, Faculty of Science, Department of Mathematics and Statistics, N-9037 Tromsø, Norway
[2]Poseidon Simulation AS, N-8376 Leknes, Norway
[3]Los Alamos National Laboratory, Los Alamos, NM 87545, USA

Received: 24 September 2001 – Revised: 25 February 2002 – Accepted: 5 April 2002

Abstract. The geometric aspects of HF-generated Langmuir turbulence in the ionosphere and its detection by radars are theoretically discussed in a broad approach, including local modelling (damped and driven Zakharov system), basic parametric instabilities, polarization and strength of the driving electric field, and radar configurations. Selected examples of numerical results from the local model are presented and discussed in relation to recent experiments, with emphasis on recent experiments at the EISCAT facilities. Anisotropic aspects of the cavitation process in the magnetized plasma are exhibited. Basic processes of cascades and cavitation are by now well identified in these experiments, but a few problems of the detailed agreement between theory and experiments are pointed out.

1 Introduction

The outdoor experimental studies of parametric instabilities in a plasma, by transmitting powerful HF radio waves into the ionosphere and using VHF and UHF radars as diagnostics, started long ago (Carlson et al., 1972; Wong and Taylor, 1971). Experimental configurations have, up until recently, been in active use at Arecibo, Puerto Rico, and since the early 1980s at EISCAT, northern Scandinavia (Hagfors et al., 1983). Since about 1988, there has been a remarkable development of experimental techniques, leading to options of space-and time-resolved experiments with simultaneously high spectral resolution (Djuth et al., 1990; Fejer et al., 1991; Sulzer and Fejer, 1994; Kohl and Rietveld, 1996; Rietveld et al., 2000; Cheung et al., 2001; Djuth et al., 2002). This has allowed for a detailed comparison between experiments and theoretical predictions.

These studies may be said to occupy a position between controlled laboratory experiments and geophysical observations. DuBois et al. (1996) discuss connections between these experiments and studies of parametric processes occurring in laser experiments. In the addition, these studies may open the road to using radars in studies of naturally occurring Langmuir turbulence in the ionosphere (Forme, 1999).

Early saturation theory was based on weak turbulence formalism (Perkins et al., 1974; Fejer and Kuo, 1973; Rypdal and Craigin, 1979; Das et al., 1985). Recent theoretical efforts have been based on numerical solutions to full wave models of the Zakharov type with damping and parametric drive included (Nicholson et al., 1984; DuBois et al., 1990, 1991; Hanssen et al., 1992; Hanssen, 1992; Sprague and Fejer, 1995; DuBois et al., 1993a, 2001). This allows for the inclusion of phenomena not describable in weak turbulence theory (e.g. cavitation) and also for a more precise description of the phenomena that weak turbulence theory includes, such as cascading.

A main issue of debate in the early stage of the period after 1988 was the mutual role of cavitation and cascade (Stubbe et al., 1992a, b; DuBois et al., 1992). Theoretically, a picture emerged (Hanssen et al., 1992; DuBois et al., 1993a, 2001) that cascading was to be expected in most of the height range below the O-mode reflection height, but that near the reflection height, Langmuir cavitation was to be expected. Predictions of radar spectral features resulting from the numerical studies (DuBois et al., 1988, 1990; Hanssen et al., 1992), were confirmed qualitatively in experiments at Arecibo (Fejer et al., 1991; Sulzer and Fejer, 1994; Cheung et al., 1989, 1992, 2001) and later also at Tromsø (Kohl and Rietveld, 1996; Isham et al., 1999b; Rietveld et al., 2000; Djuth et al., 2002), thus, strongly supporting the existence of Langmuir cavitation in these experiments.

However, these numerical studies still had several limitations: the one-dimensional model used by Hanssen et al. (1992) is very useful for obtaining an overall view of the parameter dependencies of features of HF driven Langmuir turbulence, but the geometric aspects of the observability of the turbulence cannot be addressed in such a model. The two-dimensional studies of DuBois et al. (1990, 1991, 1993a, 2001) were confined to the case where the driving electric field is polarized along the ambient magnetic field, which

Correspondence to: E. Mjølhus (einarm@mat-stat.uit.no)

is relevant for the case of the Arecibo experiments; in the EISCAT experiments other polarizations must also be considered.

The present paper is devoted to two main issues which are somewhat interrelated: (i) numerical results will be presented for the first time for the case when the electric field polarization is off-parallel , and (ii) more generally, the radar observability of the HF driven Langmuir turbulence will be a central issue. The latter is connected to the relation between the directions of the radar line of sight and the electric field polarization. The appropriate 2D driven and damped Zakharov model, including the ambient magnetic field and allowing for arbitrary polarization of the pump electric field (in the magnetic meridian plane), will be formulated and discussed in Sect. 2. In Sect. 3, the geometric aspects of the growth rates of the parametric instabilities contained in the model are discussed. In order to predict the competition between cascading and cavitation, the relative magnitude of the growth rates of the parametric decay instability (PDI) and the "oscillating two-stream instability" (OTSI) appears to be crucial (Hanssen et al., 1992; Shapiro and Shevchenko, 1984); Two-dimensional aspects of this will be highlighted. In Sect. 4, the geometric issue of observability is discussed. In the actual experiments, oblique (with respect to the vertical) radar lines of sight as well as HF incidence are often used. A simple ray tracing model is used to infer the actual configurations of angles of incidence, electric field amplitude and polarization, and radar line of sights, in the active experiments. In particular, a study of the swelling at oblique incidence, as well as the locus of the turning point outside of the spitze, is presented. In Sect. 5, a collection of examples of numerical runs of the 2D model is presented. In particular, interesting results in the cavitation range, at high values of the magnetic parameter, are presented. In this parameter range, the cavitation process tends to become more similar to the 1D case. In Sect. 6, the current status between theory and experiments is discussed, with emphasis on recent experiments at the EISCAT facilities. Some problems with the current theoretical understanding of these experiments are indicated.

2 Model

The basic features behind the choice of Zakharov-like models for the HF driven Langmuir turbulence in the ionosphere are the following two inequalities:

$$\frac{m}{M} \ll 1 \tag{1}$$

$$\frac{v_{te}}{c} \ll 1\,. \tag{2}$$

In Eq. (1) m, M are the electron and ion masses, respectively, in Eq. (2), $v_{te} = (\kappa T_e/m)^{1/2}$ is the electron thermal velocity, κ is the Boltzmann constant, T_e is the electron temperature, and c is the speed of light. Equation (1) is the basis for separation of time scales; both experiments and general theoretical considerations lead to the understanding that the nontrivial processes take place on a time scale characteristic of ion motion; then the equations of motion can be averaged over the period of the transmitted pump wave, since only the electrons can respond on that time scale, with the result that the electron nonlinearities are collected in the ponderomotive force. Equation (2) is likewise the basis for the separation of spatial scales: Eq. (2) characterizes the ratio between a typical wavelength of an electrostatic wave and an electromagnetic wave; confining attention to an electrostatic turbulence, the electrostatic approximation is introduced for the high frequency electric field, leading to a scalar equation; then Eq. (2) allows for the electric field of the electromagnetic pump wave to be represented as spatially constant.

In the first place, these assumptions imply that the electric field can be represented as

$$\mathbf{E} = \frac{1}{2}\left[(\mathbf{E}_0 + \nabla\Psi)\exp(-i\omega_0 t) + \text{c.c.}\right], \tag{3}$$

where $\mathbf{E}_0$ is constant and Ψ is varying slowly with t relative to time scale $1/\omega_0$. Then, in order for this to be true, one must also have the inequalities

$$\begin{aligned} &\frac{n}{n_0} \ll 1 \quad k^2\lambda_D^2 \ll 1 \\ &Y^2 \ll 1 \quad (\omega_0 - \omega_{pe})/\omega_0 \ll 1 \\ &\frac{v_{ce}}{\omega_0} \ll 1 \end{aligned} \tag{4}$$

In Eq. (4), n_0 is the background electron density and n is its perturbation; k is a typical Langmuir wave number and λ_D the Debye length; $Y = \Omega_{ce}/\omega_0$ with Ω_{ce} the electron gyrofrequency; $\omega_{pe} = (4\pi e^2 n_0/m)^{1/2}$ is the electron plasma frequency, where e is the magnitude of the electron charge, and v_{ce} is the effective frequency of the collisions of electrons with heavy particles. The inequalities (4) can all be seen as assumptions that perturbations of the Langmuir dispersion relation around the basic cold plasma dispersion relation $\omega = \omega_{pe}$ be small. In order to satisfy the condition on the density perturbation in Eq. (4), the (total) electric field must satisfy

$$\frac{E^2}{4\pi n_0 \kappa T_e} \ll 1\,. \tag{5}$$

These assumptions then lead to the following set of equations (see DuBois et al. (1995) for a comprehensive derivation):

$$\begin{aligned} &\nabla\cdot\left[i(\partial_t + \nu_e *) + (\Omega - n) + \nabla^2\right]\nabla\Psi - \Omega_B\nabla_\perp^2\Psi \\ &\quad = \mathbf{E}_0\cdot\nabla n \end{aligned} \tag{6a}$$

$$(\partial_t^2 + 2\nu_i * \partial_t - \nabla^2)n = \nabla^2|\nabla\Psi + \mathbf{E}_0|^2\,. \tag{6b}$$

Equations (6) are written in their dimensionless form; the units

$$\hat{T} = \frac{3}{2\eta}\,\frac{M}{m}\,\frac{1}{\omega_0} \tag{7a}$$

$$\hat{X} = \frac{3}{2}\left(\frac{M}{m\eta}\right)^{1/2}\lambda_D \tag{7b}$$

$$\hat{E}_c = \eta\left(\frac{m}{M}\right)^{1/2}\left(\frac{64\pi n_0 \kappa T_e}{3}\right)^{1/2} \tag{7c}$$

$$\hat{n}_c = \left(\frac{4\eta m}{3M}\right) n_0 \tag{7d}$$

for time, space, electric field and density are uniquely determined by the requirement that the coefficients of the classical undriven, undamped version of the Zakharov system (Zakharov, 1972) be unity. In Eq. (7), $\eta = 1 + \gamma_i T_i/T_e$, where $T_{e,i}$ are the background temperatures of electrons and ions, and γ_i is the polytropic exponent of the ions, $\lambda_D = v_{te}/\omega_{pe}$ is the Debye length. For the nondimensional quantities n and Ψ of model (6), the inequalities (4), (5) give

$$\frac{4\eta}{3}\,\frac{m}{M}\,n \ll 1$$
$$\frac{4\eta}{3}\,\frac{m}{M}\,|\nabla\Psi|^2 \ll 1. \tag{8}$$

Effects from linearized kinetic plasma theory are buried in the damping operators ν_e and ν_i. In the Fourier-transformed version of the equations, they are represented as multiplication by functions of $\mathbf{k}$. For the damping rate of Langmuir waves, we use

$$\nu_e = \nu + \nu_L(\mathbf{k}) \qquad \nu = \frac{1}{2}\,\nu_{ec}, \tag{9}$$

where ν_{ec} is the frequency of collisions between electrons and heavy particles (in the units of Eq. (7)), while $\nu_L(\mathbf{k})$ is the Landau damping rate,

$$\nu_L(k) = \left(\frac{\pi}{8}\right)^{1/2}\left(\frac{3}{2}\right)^4\left(\frac{M}{\eta m}\right)^{5/2}\frac{1}{|k|^3}$$
$$\cdot\exp\left(-\frac{9}{8}\,\frac{M}{\eta m}\,\frac{1}{k^2} - \frac{3}{2}\right). \tag{10}$$

For k beyond the maximum value of Eq. (10), the Landau damping rate $\nu_L(k)$ is, for numerical reasons, continued smoothly as ck^2, as in earlier 2D, as well as 1D simulations (e.g. DuBois et al., 1990; Hanssen et al., 1992). This is based on simulation studies of the burnout process (Dyachenko et al., 1991).

For the damping rate of ion-acoustic waves, we neglect collisional damping, while for the Landau damping, we use the formula

$$\nu_i(\mathbf{k}) = \nu_{i0}|\mathbf{k}|\,, \tag{11}$$

which is the form valid for unmagnetized plasma, where ν_{i0} is a constant.

The input parameters of this model are listed in Table 1. We comment on their significance as follows.

Table 1. Input parameters to the model

$\Omega = (\omega_0 - \omega_{pe})\hat{T}$	mismatch
$\mathbf{E}_0$ (in units of $\hat{E}_c$)	drive
$\Omega_B = \frac{1}{2}(\Omega_{ce}^2/\omega_0)T$	anisotropy
$\nu = \frac{1}{2}\nu_{ec}\hat{T}$	electron collisions
ν_{i0}	ion Landau damping parameter
M/m	mass ratio

The mismatch parameter Ω can also be interpreted as a height relative to the critical height (i.e. O-mode reflection height), assuming horizontal stratification and a smoothly varying density increasing with height; then Ω increases from zero when moving downwards from the critical height. Emphasis on the dependence of the dynamics on this parameter has been crucial in the recent comparison between theory and experiment (Hanssen et al., 1992; DuBois et al., 1993b, 2001).

The drive $\mathbf{E}_0$ is in our 2D model a two-dimensional vector with complex components. Since the phase is arbitrary (i.e. the phase of $\mathbf{E}_0$ is inherited by $\nabla\Psi$), $\mathbf{E}_0$ contains three real parameters. The two space dimensions will be assumed to span the magnetic meridian plane. For a progressive O-polarized wave, those two components of the electric field are in phase, and thus, $\mathbf{E}_0$ will contain two real parameters only. However, also including the reflected wave, at the same time as oblique incidence is allowed for, an allowance for an imaginary part of one of the components of $\mathbf{E}_0$ can take care of the combined effect of relative phase and different polarization between the upgoing and downgoing pump wave. We have not included examples with different phase in the two components of $\mathbf{E}_0$ in Sect. 5.

The magnetic field enters our model through the term in Eq. (6a) containing the anisotropy parameter Ω_B. In order for our model to be valid, the weak magnetic field condition $Y^2 \ll 1$ listed in Eq. (4) should be satisfied. Many terms of relative order Y^2 have been neglected in Eqs. (6): in the ponderomotive force (right-hand side of Eq. (6b), in the ion-acoustic response (left-hand side of Eq. (6b)), in the kinetic damping terms $\nu_i(\mathbf{k})$, $\nu_L(\mathbf{k})$, and so on. However, it should be noted that Eq. (6b) loses validity in a small range of $\mathbf{k}$ nearly perpendicular to the magnetic field. The assumption of Y^2 will only be weakly satisfied in the experimental situation; typically $1/3 > Y > 1/5$. Therefore, the parameter Ω_B will take large values under typical experimental conditions. The significance of this parameter will be of primary attention in the present work.

The collisional damping parameter ν takes values typically in the range $0.1 < \nu < 1.0$. Experience from studies of the 1D model point towards this parameter as crucial for the deviation between classical weak turbulence theory and our present "full wave" theory. Namely, at values of ν that are not too small, there will be a maximum number of cascades

as $|\mathbf{E}_0|$ increases, where the last cascade occurs far before the "Langmuir condensate" is reached. It should also be noted that it is only the Langmuir damping that accounts for the energy dissipation within this model (see the end of this section).

The ion Landau damping parameter ν_{i0} will depend crucially on the temperature ratio T_i/T_e. In Hanssen et al. (1992), a formula valid at small values of this ratio was used. Actually, the problem of choosing an appropriate value for ν_{i0} is strongly connected to one of the major weaknesses of the model (6). It is clear that the kinetic description of the ion response cannot be approximated asymptotically by an equation of the form (6b) unless the temperature ratio $T_i/T_e \ll 1$ (Stubbe et al., 1992a). One possibility is to determine the ion-acoustic dispersion relation, which is generally specified by a Landau damping rate with the dependence (11) on k, and a phase velocity. Indeed, Eq. (6b) reproduces the correct functional form of the ion-acoustic dispersion relation in the unmagnetized and quasi-neutral limit $1/\Omega_{ci} \gg \tau \gg 1/\omega_{pi}$, where τ is a characteristic time of the process. However, important processes contained in the model do not satisfy the ion-acoustic dispersion relation; this is the case for the OTSI instability. DuBois et al. (1995) and Sprague and Fejer (1995) chose the value of ν_{i0}, as well as the parameter η entering the normalizations (7), so as to represent the correct relation between the thresholds of OTSI vs. PDI. This leads to a value $\nu_{i0} = 0.49$ when $T_i/T_e = 1$, which is considerably larger than that used in earlier work (e.g. Hanssen et al., 1992). In DuBois et al. (1995), this was called the "best fit two-pole approximation". By choosing ν_{i0} in this way, Sprague and Fejer (1995) obtained from the model coexisting features of PDI and OTSI which had been observed in experiments (Kohl and Rietveld, 1996), but which were not obtained in the earlier 1D simulations (Hanssen et al., 1992, Hanssen, 1992). This choice cannot simultaneously be expected to represent a fair competition between the growth rates of the two instabilities. On the other hand, the general features of them, such as the qualitative aspects of their dependence on $E_{0,\theta}$ versus $\Omega_{0,\theta}$ (see next section) will be retained. In general, ν_{i0} should be chosen in the interval $0.1 < \nu_{i0} < 0.5$, increasing with the ratio T_i/T_e.

In DuBois et al. (1995), a three-pole approximation was also tested. This builds on an idea of Hammet and Perkins (1990). In its original form transferred to replace Eq. (6b), the three-pole approximation of Hammet and Perkins (1990) did not provide a good representation of thresholds and growth rates of the parametric instabilities contained in Eq. (6). DuBois et al. (1995), therefore, introduced a "best fit three-pole approximation". Numerical comparison between this and the "best fit two-pole approximation" (as described above) in DuBois et al. (1995), showed good qualitative similarity between the two.

The mass ratio M/m enters significantly in the definitions of the parameters of Table 1. If Langmuir Landau damping were neglected (as would be appropriate in most of the cascading range), then the mass ratio would not enter the model in any other way. However, it is seen from

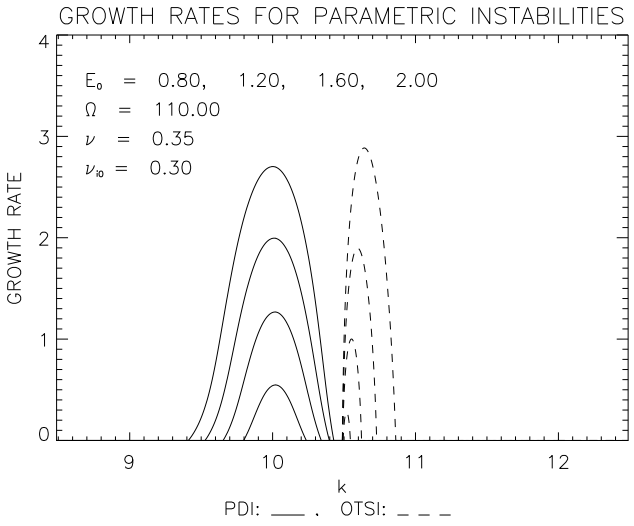

Fig. 1. Example of growth rates for the parametric instabilities. Solid lines for PDI and dashed lines for OTSI, for four values of $E_{0,\theta}$.

Eq. (10) to enter strongly in the Landau damping. For parameter values where cavitation occurs, Landau damping is crucial. Therefore, wave numbers ranging up to the Landau damping range $k_L \sim 1/\lambda_D$ must be contained in the numerical model. On the other hand, the cascading steps have wave number decrements $\Delta k = 1/\hat{X}$. The numerical wave number space must resolve these intervals well. Consequently, the number of Fourier modes $n_x \times n_y$ must satisfy $n_{x,y} \gg 2k_L/\Delta k \sim 3\sqrt{M/(\eta m)}$ (the factor 2 arises, because both positive and negative must be included). This requirement on the number of modes in most cases also ensures that the fairly narrow wave number ranges of the parametric instabilities are well resolved in the numerical model. The latter is very important; as an example, refer to Fig. 1: if the numerical wave number space does not hit near the maxima of the growth rates, the instabilities, as well as their mutual competition, might be misrepresented in the numerical model. Figure 1 will be further explained in Sect. 3.

In order to resolve this dilemma, the model (6) has often been run numerically for reduced values of the mass ratio, meaning that the correspondence between the parameters of Table 1 and an assumed real situation is computed for a reduced value of M/m. Examples are DuBois et al. (1988, 1990, 1991, 1995, 2001), while in the 1D work of Hanssen et al. (1992), realistic mass ratio was retained. For example, in the recent paper by DuBois et al. (2001), the mass ratio was chosen as 6200, which is about one-fifth of a realistic (O^+) value. Features such as the thresholds for the actual parametric instabilities (Eqs. (23) and (28) below) scale independent on the mass ratio; the same is true for the angular growth range Eq. (32). Regarding growth rates, the approximate versions (25) and (30) below scale independent of the mass ratio, while Eq. (26) does not. The transition from cascading to cavitation is expected to depend on mass ratio, so that reduced mass ratio favours cascading: for example,

rescaling the points on the broken line on Fig. 27 of Hanssen et al. (1992), with reduced mass ratio, will bring them into the cascading range. In this paper, efforts are made to retain parameters corresponding to realistic mass ratio, and the mode number is chosen accordingly.

The numerical method by which Eq. (6) is integrated is an integral part of the modelling. Periodic boundary conditions are used, implying that physics can go on in a system of finite size, but still without boundaries. This makes our model a local model, where the background state is constant, specified by the choice of values of the parameters of Table 1. The periodic boundary conditions then allow for optimized, two-dimensional fast Fourier transform routines to be used. Periodic boundary conditions are physically acceptable provided the dimensions of the simulation cell are large compared to the intrinsic correlation lengths of the turbulence, as measured by the inverse width in k space of the dominant spectral features. For example, the size of the simulation cell L must be large enough that the resolution in k space $2\pi/L \ll \Delta k$, where Δk is the width of the cascade lines, as discussed above in the context of mode number requirement.

The model described above is rich in dynamical behaviour, having a large parameter space, and no doubt, many aspects of the observed behaviour in the actual radio experiments is contained qualitatively in it. Even so, there is obviously important physics left out of it. Among the major omissions and weaknesses we list the following:

1. The constraining to two space dimensions probably constitutes the most severe simplification. There are several aspects of this:

   (a) For the cavitation range, the dimensionality is important, both for the nucleation phase and the collapse phase. In 1D, nucleation is easy, while inertial collapse, wherein the cavitation asymptotically decouples from the heater field, does not exist but directly driven collapse is observed instead. Even so, numerical studies show that energy is transferred in k space to the Landau damping range also in this case (Hanssen et al., 1992; Hanssen, 1992). In 2D, numerics indicate that nucleation takes place less frequently, while inertial collapse now comes into existence. For 3D, numerical studies have been possible only with very poor wave vector space resolution (Robinson et al., 1988). It is expected that the trend from 1D to 2D continues when passing from 2D to 3D. For example, collapse in 2D requires a threshold for the trapped energy, but not in 3D. Though, see our discussion of cases with large Ω_B in Sect. 5, indicating that in the magnetized case, things become more similar to 1D.

   (b) Constraining the excited dynamics to the magnetic meridian plane, implies constraining out parametric excitation by the component of the electric field perpendicular to this plane. The latter is in quadrature with the component in the magnetic meridian plane.

2. The reaction of the electron distribution function on the turbulence represents important physics left out of our present model. In the cavitation range, this is probably a very important feature: all particle simulations of HF generated Langmuir turbulence show that the electron distribution is perturbed by the Langmuir turbulence; thus, an energetic tail on the electron distribution will be formed. Recent reduced particle-in-cell simulations in Sanbonmatsu et al. (2000) indicate that for weakly driven systems, the fast particle acceleration has a negligible effect on the turbulence levels and spectra. For more strongly driven cases, the turbulence levels are suppressed by increased Landau damping. One alternative is to represent this by updating the electron distribution by a quasi-linear velocity space diffusion model, as has recently been done (Sanbonmatsu et al., 1999, 2000). On the other hand, this type of modelling is complicated by the intrinsic nonlocality of the problem; assuming that cavitation takes place in a thin layer in the vicinity of the O-mode reflection level, accelerated particles may leave this layer, but subsequently some of them may return after collision with heavy particles (Gurevich et al., 1985).

3. The locality of the model: the feature of accelerated electrons is already mentioned; here, we focus on other aspects of this. In the model (6), the background state is defined by a set of parameter values (cf. Table 1). However, these values are space dependent in the experimental situation. This is in particular true for the electric field $\mathbf{E}_0$, the scale of which is given by the O-mode wavelength. Also, the spatial variation of Ω may be important. The local model is justified if the mesoscopic variation of the background parameters, such as the density profile and the heater interference pattern, vary on scales large compared to the correlation lengths of the turbulence. In this case the predicted radar spectrum can be represented as an incoherent sum of the locally computed spectra over the observed altitudes. In the cascading range, different states will be coupled by Langmuir propagation, which is limited by Langmuir linear damping. In the cavitation regime, the spectra are broad, indicating small correlation lengths; here, the local approximation should be excellent. Accelerated electrons are also a potential mechanism of nonlocal coupling in all regimes. The recent resolved altitude ordering of the observed turbulence (Rietveld et al., 2000; Cheung et al., 2001; Djuth et al., 2002) indicates that the local approximation is, in fact, valid, even in the cascading regime.

4. The inadequacy of our representation of the effects of the magnetic field for wave vectors nearly perpendicular to the magnetic field has been mentioned above.

5. The inadequacy of the representation of the kinetic description of the ion dynamics has been mentioned above and is discussed by Stubbe et al. (1992b) and DuBois et al. (1995). A 1D numerical study with linearized Vlasov dynamics of the ions has been presented by Helmersen and Mjølhus (1994); it showed the same qualitative features as obtained in the 1D Zakharov model, although a bias towards the cavitation regime was found. Vlasov simulations (Wang et al., 1994, 1995) and reduced particle-in-cell simulations (Sanbonmatsu et al., 1999, 2000) with particle electrons and ions have shown the same qualitative features as predicted by the Zakharov model and in some weakly driven cases, quantitative agreement between the models was obtained as mentioned above.

The driven and damped character of the model (6) should be emphasized, as opposed to the conservative version (Zakharov, 1972) often emphasized in earlier work. The drive represented by $\mathbf{E}_0$ is clearly exhibited when the energy balance equation for the model is written up. Using the procedure on p. 17 530 of Mjølhus et al. (1995), the balance

$$\frac{d}{dt}\bar{U} = \bar{W} - \bar{D} \tag{12}$$

can be obtained, where

$$\bar{U} = \frac{1}{2}\int_{T^2} |\nabla\Psi|^2 d\mathbf{x} \tag{13}$$

is the electrostatic energy in the simulation cell T^2,

$$\bar{D} = \frac{1}{2}\int_{T^2} \left[\nabla\Psi \cdot (\nu_e * \nabla\Psi^*) + \text{c.c.}\right] d\mathbf{x} \tag{14}$$

the dissipation, and

$$\bar{W} = \frac{1}{2} i\mathbf{E}_0^* \cdot \int_{T^2} n\nabla\Psi d\mathbf{x} + \text{c.c.} \tag{15}$$

is the Joulean energy injection into the cell (Doolen et al., 1985). The energy loss from the incident radio wave is a global effect that is not represented in the local model (6); instead, a spatial damping on a global scale can be accounted for (Mjølhus et al., 1995).

3 The dispersion relation

The feature of external drive, represented by the complex vector $\mathbf{E}_0$, implies that the unperturbed state $n = 0, \nabla\Psi = 0$ may be unstable, typically when $|\mathbf{E}_0|$ is above some threshold. The instabilities, the parametric decay instability (PDI), and the "Oscillating Two-Stream Instability" (OTSI), are well-known. However, the dispersion relation leading to these instabilities from the model (6) is quite complex, and so we discuss here some useful approximate formulas and general features.

In particular, it is intended to exhibit explicitly the dependence of the modes on the geometric features. Fortunately, the basic formulation of this aspect is rather simple: stability is investigated by considering plane wave solutions of the linearization of Eqs. (6); however, plane wave implies 1D spatial variation, so one will come to the same result by considering the constraining of Eqs. (6) to dependence on one spatial direction, and thereafter, linearize and Fourier analyze. A unit vector in this direction is denoted by $\mathbf{e}_\xi$, and the spatial coordinate in that direction is denoted by ξ. Then, the system of Eqs. (6) is readily brought into the form

$$\left[i(\partial_t + \nu*) + (\Omega_\theta - n) + \partial_\xi^2\right] E = E_{0,\theta} n - i j_2 \tag{16a}$$

$$(\partial_t^2 + 2\nu_i * \partial_t - \partial_\xi^2) n = \partial_\xi^2 |E + E_{0,\theta}|^2 \tag{16b}$$

after one integration of Eq. (6a). Here, $E = \partial_\xi \Psi$, $j_2 = -i\langle nE\rangle$ (spatial average) can be considered as a constant of integration (for example, necessary to make Ψ well-defined on our periodic numerical model), and

$$E_{0,\theta} = \mathbf{E}_0 \cdot \mathbf{e}_\xi \tag{17a}$$

$$\Omega_\theta = \Omega - \Omega_B \sin^2\theta\ , \tag{17b}$$

where θ is the angle between the direction $\mathbf{e}_\xi$ and the external magnetic field. It is seen that Eq. (16) has the form of a 1D Zakharov system, such as, for example, considered in Hanssen et al. (1992); the geometric features enter only through the parameters $E_{0,\theta}$ and Ω_θ of Eq. (17). In particular, $E_{0,\theta}$ can now be considered real and positive, with no loss of generality, because any phase can be absorbed into E. For the case of $\mathbf{E}_0$ real (i.e. the two components in phase), one has

$$E_{0,\theta} = E_0 \cos(\alpha - \theta)\ , \tag{18}$$

where α is the angle between $\mathbf{E}_0$ and the magnetic field direction. Linearizing Eq. (16) around the vanishing state and subsequently Fourier analyzing as $\sim \exp[i(k_\theta\xi - \omega t)]$, the quartic dispersion relation

$$P_0(\omega) = 2k_\theta^2 \mu E_{0,\theta}^2 \tag{19}$$

with

$$P_0(\omega) = \prod_{j=1}^{4} (\omega - \omega_{0j})\ , \tag{20}$$

where

$$\omega_{01} = \mu - i\nu$$
$$\omega_{02} = -\mu - i\nu$$
$$\omega_{03} = ck_\theta - i\nu_{i0}|k_\theta|$$
$$\omega_{04} = -ck_\theta - i\nu_{i0}|k_\theta|$$
$$c = \sqrt{1 - \nu_{i0}^2}$$
$$\mu = k_\theta^2 - \Omega_\theta$$

is obtained. Details in the process of obtaining Eq. (19) are omitted; however, we mention the following: equation (16a) constitutes two real equations for the real and imaginary parts of E; when Fourier analyzing, these two quantities must be

represented independently by complex amplitudes. Alternatively, one can treat E and E^* (complex conjugate) as independent. E^* is then often referred to as the "anti Stokes component".

In Eq. (19), we consider ω as unknown, and k, Ω_θ, $E_{0,\theta}$, ν and ν_{i0} as parameters. In general, the 4 roots of Eq. (19) have a complicated dependence on these parameters. In the limit $E_{0,\theta} = 0$, we have the roots $\omega = \omega_{0j}$, $j = 1, ..., 4$, which represent the Langmuir wave described by E (ω_{01}), the Langmuir wave described by E^* (ω_{02}), and the forwards and backwards propagating sound wave (ω_{03} and ω_{04}). The Langmuir mode propagates forwards (backwards) when $k > 0$ (< 0).

Instabilities, i.e. positive values of the imaginary part of the roots of Eqs. (19) and (20), exist near values of k for which the real parts of ω_{0j} coalesce. The PDI, with right-moving Langmuir wave and left-moving ion-acoustic wave, occurs when $\mathrm{Re}(\omega_{01}) = \mathrm{Re}(\omega_{04})$, e.g. $k_\theta^2 - \Omega_\theta + ck_\theta = 0$, $k_\theta > 0$, also implying $\mathrm{Re}(\omega_{02}) = \mathrm{Re}(\omega_{03})$, which gives

$$\hat{k}_\theta = -\frac{c}{2} + \sqrt{\Omega_\theta + c^2/4}\,. \tag{21}$$

Similarly, for the left-moving Langmuir wave ($\hat{k}_\theta < 0$) and the right-moving ion-acoustic wave, the resonance condition is $\mathrm{Re}(\omega_{01}) = \mathrm{Re}(\omega_{03})$, leading to the negative of Eq. (21). For these two situations, $\mu < 0$, implying a negative frequency shift, a well-known property of parametric instabilities of decay type.

The OTSI occurs near values of k, for which ω_{01} and ω_{02} are both zero, i.e. $\mu = 0$. At the exact value $\mu = 0$, the coupling term (i.e. the right-hand side of Eq. (19)) again vanishes, so for that value of k the roots are the modes ω_{0j}, which are all damped. As it turns out, this instability exists for a range of values of k_θ for which $\mu > 0$. In Fig. 1, an example of the growth rates of each of them as a function of k at increasing values of $E_{0,\theta}$ are plotted, as computed from Eq. (20). The growth ranges, i.e. the range of k with positive growth rate, are seen to be relatively narrow. More useful: the point $\mu = 0$ cannot be in any of the growth ranges for the reason stated above; therefore, this condition separates the growth ranges of the two instabilities. This is a useful criterion to identify the two instabilities when solving Eq. (19) numerically.

From Fig. 1, the competition between the two instabilities is also seen; the OTSI has the largest threshold, but its growth rate increases more rapidly with $E_{0,\theta}$, so that it wins at higher values, at least at sufficiently small values of Ω_θ.

In order to obtain useful formulas for the two instabilities, a natural approximation is to substitute the resonance condition into the two non-resonant factors on the left-hand side of Eq. (19); this will give quadratic equations for the growth rates. Consider first the PDI. Assuming the resonance condition, implying Eq. (21), put $\omega = \mu = -c\hat{k}_\theta$ and neglect damping in the two nonconfluent factors of (19), and $\omega = \mu + i\gamma = -c\hat{k}_\theta + i\gamma$ in the confluent factors; this gives

$$\gamma^2 + \left(\nu + \nu_{i0}|\hat{k}_\theta|\right)\gamma - \left(\frac{1}{2}\,\hat{k}_\theta\,\frac{E_{0,\theta}}{c} - \nu\nu_{i0}|\hat{k}_\theta|\right) = 0\,. \tag{22}$$

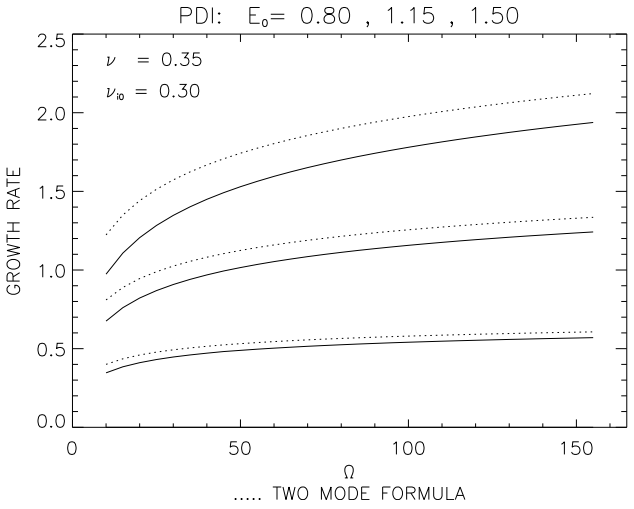

Fig. 2. Example of maximum growth rates for the PDI instability as a function of Ω_θ for three different values of $E_{0,\theta}$. Dashed lines show result from using two-mode formula.

For $E_{0,\theta} > E_{0,t}$, where

$$E_{0,t}^2 = 2c\nu\nu_{i0}\,, \tag{23}$$

Eq. (22) has one positive (and one negative) real root; thus, $E_{0,t}$ is the threshold value in approximation (22). This threshold is not an exact result from Eq. (19), although it is a very good approximation in most situations. The true threshold increases somewhat when Ω_θ decreases. For $E_{0,\theta}$ above this threshold, the maximum growth rate according to Eq. (22) is

$$\gamma_{M,PDI} = -\frac{1}{2}\,\nu_{i0}|\hat{k}_\theta| + \sqrt{\frac{1}{2}\,\frac{\hat{k}_\theta(E_{0,\theta}^2 - E_{0,t}^2)}{c} + \frac{1}{4}\,\nu_{i0}^2|\hat{k}_\theta|^2}\,, \tag{24}$$

where $\nu \ll \nu_{i0}|k|$ was assumed. Just above the threshold, the second term under the square root will dominate, and one has the simplified formula

$$\gamma_{M,PDI} \simeq \frac{1}{2}\,\frac{(E_{0,\theta}^2 - E_{0,t}^2)}{c\nu_{i0}}\,. \tag{25}$$

In the opposite limit: far above threshold, one has the simplified formula

$$\gamma_{M,PDI} \simeq \left(\frac{1}{2}\,\hat{k}_\theta\,\frac{E_{0,\theta}^2}{c}\right)^{1/2} - \frac{1}{2}\,\nu_{i0}|\hat{k}_\theta|\,. \tag{26}$$

A closer inspection shows that the two-mode approximation (22) requires $E_{0,\theta}^2/\hat{k}_\theta \ll 1$. In Fig. 2, we show the PDI growth rate as a function of Ω_θ, for 3 values of $E_{0,\theta}$, and compare it with the two-mode formula (24).

In the above formulas, k_θ was kept fixed at the value $\hat{k}_\theta$ of confluence, and it was tacitly assumed that this gives the maximum growth rate for the chosen direction θ. A closer

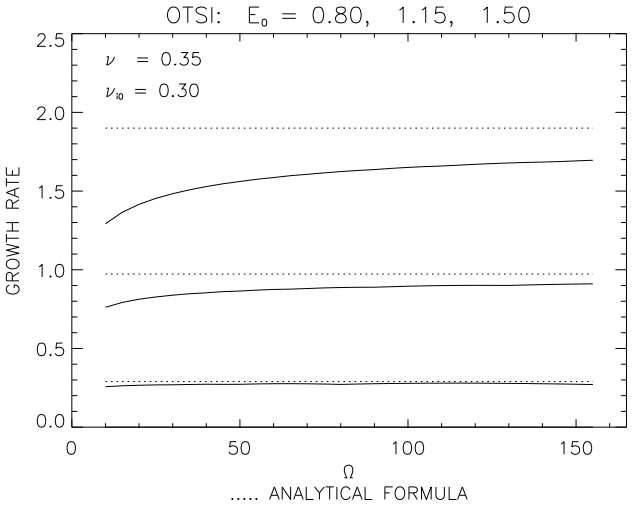

Fig. 3. Example of maximum growth rates for the OTSI instability as a function of Ω_θ for three different values of $E_{0,\theta}$. Dashed lines show result from using two-mode formula.

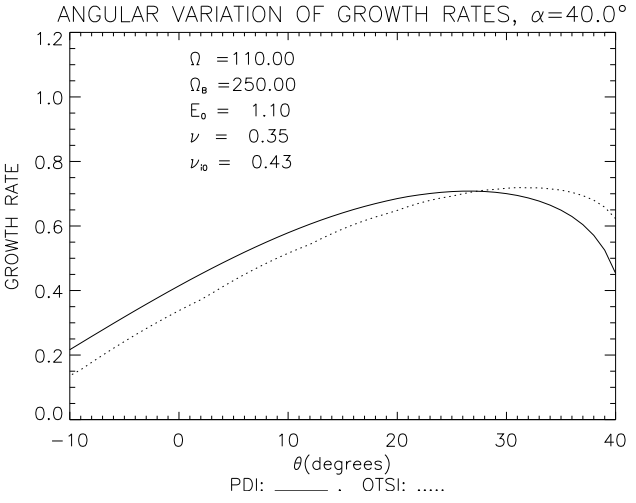

Fig. 4. Example of maximum growth rates for the OTSI and PDI instability as a function of θ for $\alpha = 40$ and $\nu_{i0} = 0.45$. Dashed line shows OTSI growth rate and solid line shows PDI growth rate.

numerical study showed that this is an excellent approximation, although apparently neither is fully exact.

For the OTSI instability, one can analyze Eq. (19) as follows: first, substituting $\omega = i\gamma$, the left-hand side becomes a polynomial with real-valued coefficients. Next, a condition for the constant term to vanish is

$$\nu^2 + \mu^2 - 2\mu E_{0,\theta}^2 = 0\,. \tag{27}$$

At values of k where this is satisfied, the dispersion relation has a root $\gamma = 0$. Assuming this is a simple root $\gamma(k)$ which has $\partial_k \gamma \neq 0$, there will be values of k in the neighbourhood for which $\gamma(k)$ is positive (as well as negative). Thus, there is a purely growing instability. Actually, Eq. (27) defines two values of k when $E_{0,\theta} > E_{0,t}$, where

$$E_{0,t}^2 = \nu \tag{28}$$

and there is positive growth rate precisely between these values. Equation (27) clearly shows that $\mu > 0$ for this to happen. The threshold (28) is exact (within the model (6)). In order to obtain simple approximate expressions for the growth rate, we neglect again the growth rate in the acoustic factors of Eq. (19), while retaining it in the two confluent factors, giving

$$(\gamma + \nu)^2 + \mu^2 - 2\mu E_{0,\theta}^2 = 0\,. \tag{29}$$

It is readily seen that the largest growth rate occurs for $\mu = E_{0,\theta}^2$, e.g. $k_\theta = (\Omega_\theta + E_{0,\theta}^2)^{1/2}$. This gives

$$\gamma_{M,OTSI} = -\nu + E_{0,\theta}^2\,. \tag{30}$$

In Fig. 3, the numerically computed maximum growth rate of OTSI is plotted as a function of Ω_θ, together with the results using formula (30), for three different values of $E_{0,\theta}$. It is seen that Eq. (30) is not a particularly good approximation at higher values of $E_{0,\theta}$. By comparing Figs. 2 and 3, or considering Fig. 1, it can be seen that, at the smaller values of Ω_θ and larger values of $E_{0,\theta}$, the OTSI may have a larger growth rate than the PDI, with respect to a fixed direction. In Hanssen et al. (1992), it was concluded from numerical material that the dynamics goes to cavitation when the OTSI has the largest growth rate. An original motivation for the present study was to look for this to happen when the drive is off-parallel. For example, Ω_α may be small and $E_{0,\alpha}$ large, so that the OTSI has the largest growth rate in direction α. However, looking at direction θ with $\alpha > \theta > 0$, one sees from Eqs. (17) that Ω_θ increases while going towards smaller θ, while $E_{0,\theta}$ will decrease. This trade-off may result in PDI having the largest growth rate, occurring at an angle θ_m, $\alpha > \theta_m > 0$. In Fig. 4, we show a case where the OTSI has (slightly) the largest overall growth rate. It does not seem worthwhile to express this trade-off analytically.

The angular growth range of the PDI, defined as the range of directions θ for which the PDI has a positive growth rate, can be obtained from Eqs. (23) and (18) as

$$\alpha - \theta_c < \theta < \alpha + \theta_c\,, \tag{31}$$

where

$$\cos\theta_c = \frac{\sqrt{2\nu\nu_{i0}c}}{E_0}\,. \tag{32}$$

4 Observability: geometric aspects

Experiments where the HF-excited parametric instabilities in the ionosphere are probed by means of incoherent radars, have been performed at the Arecibo Observatory, Puerto Rico, and at the EISCAT facilities in northern Scandinavia. The Arecibo facility has a 430 MHz radar, which is usually pointed vertically, and a high power (<80 MW Equivalent

Radiated Power (ERP), 3–9 MHz) transmitter located 17 km to the northeast of the radar. The EISCAT facilities consist of a high power (<1.2 GW ERP) HF transmitter located near Tromsø, Norway, which can operate in the frequency range 3.85–8.0 MHz, and two diagnostic radars of 224 MHz (VHF) and 933 MHz (UHF). The UHF radar, in addition, has remote receivers in Kiruna, Sweden, and Sodankylä, Finland.

The radar predictions from the model (6) are made as follows:

1. Using a spectral method for generating a numerical solution to Eq. (6), it will consist of $n_x \times n_y$ time series $\Psi(t;\mathbf{k})$, $n(t;\mathbf{k})$, where n_x (n_y) are the number of Fourier modes in x (y) directions (where $\mathbf{k} = (k_x, k_y)$ takes $n_x \times n_y$ values).

2. Each radar configuration described above defines a certain wave vector $\mathbf{k}_p$ for Bragg scatter as

$$\mathbf{k}_p = \pm 2k_0 \cos\frac{\phi}{2}\,\mathbf{e}_{\phi/2} \tag{33a}$$

$$k_0 = \omega_R/c\,, \tag{33b}$$

where ω_R is the (angular) frequency of the radar, ϕ is the angle between the lines of sight of the transmitting and receiving radar to the ionospheric volume element being probed, and $\mathbf{e}_{\phi/2}$ a unit vector bisecting the angle between these lines.

3. One can then select the complex time series $\Psi(t;\tilde{\mathbf{k}}_p)$, $n(t;\tilde{\mathbf{k}}_p)$, where $\tilde{\mathbf{k}}_p$ is the (discrete) wave vector in the numerical model that best approximates $\mathbf{k}_p$, and perform a discrete Fourier transform over m selected time subintervals of equal length, and form the averaged power spectra

$$S_p(\omega) = \frac{1}{m}\sum_{j=1}^{m} |\tilde{k}_p^2 \Psi_j(\omega;\tilde{\mathbf{k}}_p)|^2 \tag{34a}$$

$$S_i(\omega) = \frac{1}{m}\sum_{j=1}^{m} |n_j(\omega;\tilde{\mathbf{k}}_p)|^2\,. \tag{34b}$$

Here, the indices p, i stand for "plasma line" and "ion spectrum", respectively. For the three radars, we are using the values $k_p = 9.38\ \mathrm{m}^{-1}$ (EISCAT VHF), $k_p = 18.01\ \mathrm{m}^{-1}$ (Arecibo), and $k_p = 39.08\ \mathrm{m}^{-1}$ (EISCAT UHF, monostatic mode). In Sect. 5, we refer to dimensionless quantities; then $k_p \mapsto \bar{k}_p = \hat{X} k_p$, where $\hat{X}$ is given in Eqs. (7).

Thus, our model is that these spectra are proportional to the contribution to the observed radar spectrum arriving from the particular ionospheric location modelled by the parameter values entered into Eqs. (6), in the "plasma line" and "ion line" bands, respectively, (DuBois et al., 1988, 1990; Hanssen et al., 1992). We shall refer to these power spectra at fixed wave vectors as "virtual radars". The ability to extract plasma line and ion line power spectra from the simulation data is perhaps the most important diagnostic in the recent approach to Langmuir turbulence and led directly to predictions of cavitating turbulence features near reflection density (DuBois et al., 1988), which were subsequently identified in experiments (Cheung et al., 1989). We note that no other approach to this problem has produced power spectra.

The theoretical prediction of observability of the HF-generated Langmuir turbulence is then related to the occurrence and strength of a Fourier component at $\tilde{\mathbf{k}}_p$ in the generated solution. This, in turn, depends on the parameters described in Sect. 2. In particular, the direction and strength of $\mathbf{E}_0$ is decisive. Of particular interest is the polarization and electric field amplitude at the matching state $X = X_{\mathrm{match}}$, where waves of frequency ω_0 and wave vector $\mathbf{k}_p$ satisfy the Langmuir dispersion relation

$$1 - X_{\mathrm{match}} = 3(\lambda_D k_p)^2 + Y^2 \sin^2\Phi_0\,, \tag{35}$$

where Φ_0 is the angle between the radar line of sight and the magnetic field direction, and $X = \omega_{pe}^2/\omega_0^2$ is the normalized plasma frequency. In the dimensionless quantities of Sect. 2, this takes the form

$$\bar{k}_p^2 + \bar{k}_p = \Omega_{\phi_0}\,, \tag{36}$$

where Ω_θ is defined in Eq. (17b) (the second term on the left-hand side of Eq. (36) is not included in Eq. (35); it represents the frequency downshift of the decay instability).

In order to describe the aspects of electric field polarization and amplitude in more detail, it was natural to refer $\mathbf{E}_0$ to two different orthonormal right-hand bases (see Fig. 5). For a description of polarization, the base $\mathbf{e}_\parallel$, $\mathbf{e}_\perp$, $\mathbf{e}_z$ is used, where $\mathbf{e}_\parallel$ is along the magnetic field direction, $\mathbf{e}_\perp$ is perpendicular to $\mathbf{e}_\parallel$, but in the magnetic meridian plane, and $\mathbf{e}_z$ is perpendicular to the magnetic meridian plane. For a description of the energy conservation and ray optics in a horizontally plane-stratified medium, $X = X(\xi)$, the base $\mathbf{e}_\xi$, $\mathbf{e}_\eta$, $\mathbf{e}_\zeta$ is more natural, where $\mathbf{e}_\xi$ points vertically, $\mathbf{e}_\eta$ points horizontally in the magnetic meridian plane, and $\mathbf{e}_\zeta = \mathbf{e}_z$. The components of $\mathbf{E}_0$ are then connected as

$$E_{0,\xi} = E_{0,\parallel}\cos\alpha_0 + E_{0,\perp}\sin\alpha_0 \tag{37a}$$

$$E_{0,\eta} = -E_{0,\parallel}\sin\alpha_0 + E_{0,\perp}\cos\alpha_0 \tag{37b}$$

$$E_{0,\zeta} = E_{0,z}\,, \tag{37c}$$

where α_0 is the angle between the vertical and the magnetic field.

The polarization relations can now be taken from Stix (1962), and read

$$E_{0,\perp} = -R E_{0,\parallel} \tag{38a}$$

$$E_{0,z} = i\sigma E_{0,\perp} \tag{38b}$$

where

$$R = \frac{1 - X - N^2\sin^2\theta}{N^2\sin\theta\cos\theta} \tag{39a}$$

$$\sigma = \frac{D}{\epsilon_\perp - N^2} \tag{39b}$$

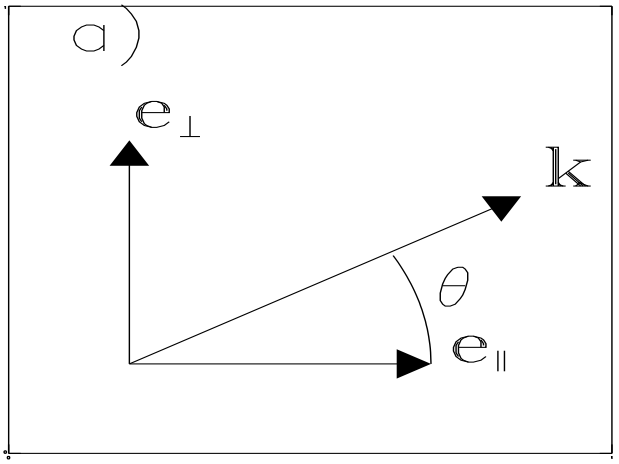

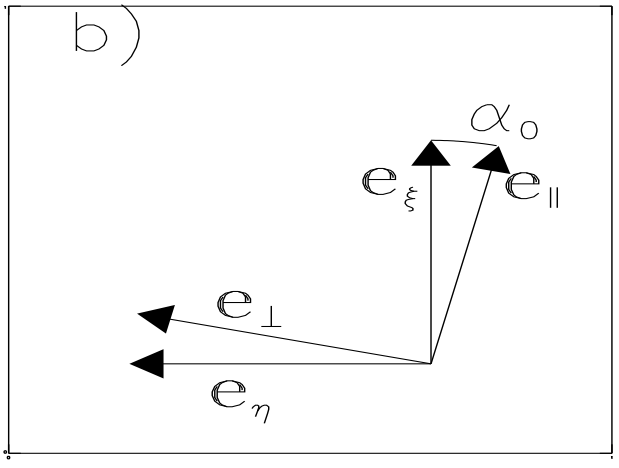

Fig. 5. Coordinate unit vectors. (a) The meaning of θ. (b) Coordinate vectors oriented with respect to vertical vs. those oriented with respect to the magnetic field.

and $\epsilon_\perp = 1 - X/(1-Y^2)$, $D = XY/(1-Y^2)$. The O-mode index of refraction N is given by

$$N^2 = 1 - \frac{X(1-X)}{1 - X - \frac{1}{2}Y^2\sin^2\theta + \Delta} \tag{40a}$$

$$\Delta = \left[(Y(1-X)\cos\theta)^2 + \left(\frac{1}{2}\,Y^2\sin^2\theta\right)^2 \right]^{1/2} . \tag{40b}$$

Here, θ has the same meaning as in Sect. 3, namely the angle between the current **k** and the magnetic field. For normal (i.e. vertical) incidence and plane-stratified medium, $\theta = \alpha_0$, otherwise θ will vary along the ray path, and will have to be determined by ray tracing.

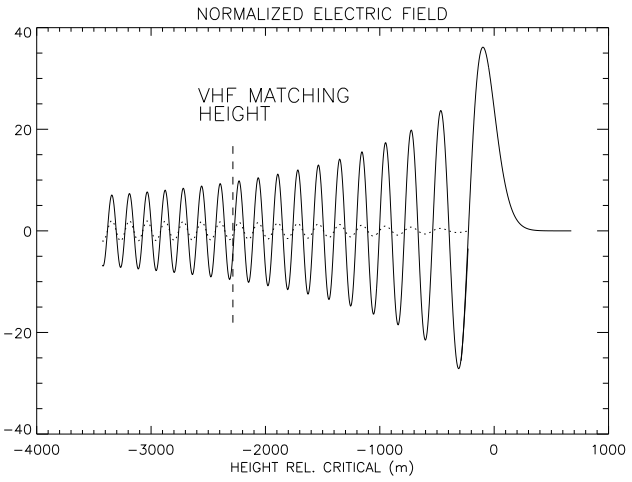

Fig. 6. Example of the spatial structure of the electric field of a normally incident radio wave just below the critical height, according to (46) and (48) (with $\hat{E}_0 = 1$). Solid line: $E_{0,\parallel}$, broken line: $E_{0,\perp}$. The parameters: $\omega_0 = 2\pi f_0$ with $f_0 = 4.544\,\mathrm{MHz}$, $\alpha_0 = 12°$, $Y = f_{ce}/f_0$ with $f_{ce} = 1.35\,\mathrm{MHz}$, and $L = 160\,\mathrm{km}$. The VHF matching height is marked according to $T_e = 0.17\,\mathrm{eV}$.

The most commonly used model to estimate the strength of $\mathbf{E}_0$ at a given location, e.g. the matching height, has the following two steps:

1. Often, the transmitter power is given as ERP (Equivalent Radiated Power). Then, at vertical height H and angle of incidence θ_0 (relative to the vertical), the vertical component of the time-averaged Poynting flux is

$$\bar{P}_\xi = \frac{Q\cos^3\theta_0}{4\pi H^2} , \tag{41}$$

   where, for simplicity, straight rays are assumed.

2. For propagation over distances much smaller than H, in the vicinity of the O-mode reflection level $X = 1$, the following model is usually adapted:
   (a) plane-stratified medium, $X = X(\xi)$, and
   (b) parallel rays, $k_\eta = \frac{\omega}{c}N_\eta = \text{const.}$, where N_η is related to the angle of incidence by $N_\eta = \sin\theta_0$.

Then, the variation of the wave amplitude is governed by the conservation of $\bar{P}_\xi$, which is given by

$$\bar{P}_\xi = \frac{c}{8\pi}\big[N_\xi(|E_{0,\xi}|^2 + |E_{0,\eta}|^2) - N_\eta\,\frac{1}{2}(E_{0,\eta}E^*_{0,\xi} + \text{c.c})\big] , \tag{42}$$

where $N_{\eta,\xi} = (c/\omega)k_{\eta,\xi}$ are the dimensionless wave vector components. Using the polarization relation (38) and the transformation (37), the components of the electric field amplitude can be expressed as

$$E_{0,\parallel} = K_\parallel \hat{E}_0 \tag{43a}$$

$$E_{0,\perp} = K_\perp \hat{E}_0 , \tag{43b}$$

where $\hat{E}_0$ is a reference electric field amplitude determined as the η component of a vacuum circularly polarized wave electric field at height H and angle of incidence θ_0, which from Eqs. (41), (42) is given by

$$\hat{E}_0 = \left(\frac{Q \cos^4 \theta_0}{cH^2} \right)^{1/2} . \tag{44}$$

(When Q is given in watts, we obtain $\hat{E}_0$ in SI units volts/m by substituting $1/c \mapsto c\mu_0/4\pi$, where $\mu_0 = 4\pi \times 10^{-7}$.) In Eq. (43), the swelling factors are given by

$$K_\parallel = \left(\frac{2}{\cos\theta_0} \right)^{1/2} K_0 \tag{45a}$$

$$K_\perp = -RK_\parallel \tag{45b}$$

$$K_0 = \Big\{ N_\xi \left[\sigma^2 R^2 + (\sin\alpha_0 + R\cos\alpha_0)^2 \right] + N_\eta (\sin\alpha_0 + R\cos\alpha_0)(\cos\alpha_0 - R\sin\alpha_0) \Big\}^{-1/2} . \tag{45c}$$

In the case of vertically incident wave, $\theta_0 = 0$, e.g. $\theta = \alpha_0$, the incident and reflected wave will overlap, and the spatial structure of the electric field should be described as

$$\begin{pmatrix} E_\parallel(\xi) \\ E_\perp(\xi) \end{pmatrix} = 2 \begin{pmatrix} K_\parallel \\ K_\perp \end{pmatrix} \hat{E}_0 \sin \left(\int_\xi^0 \frac{\omega_0}{c} N d\xi + \frac{\pi}{4} \right) , \tag{46}$$

where $K_\parallel$ of (45) in this case is given by

$$K_\parallel = \left\{ \frac{2}{N[\sigma^2 R^2 + (\sin\alpha_0 + R\cos\alpha_0)^2]} \right\}^{1/2} , \tag{47}$$

N is given by (40), and $\xi = 0$ at $X = 1$. Equations (46), (47) break down as $\xi \to 0$ ($X \to 1$), because $N \to 0$ in (47); then just below $X = 1$, (46), (47) overlap with

$$E_{0,\parallel} = 2\sqrt{2\pi} \left(\frac{\omega_0}{c} L \right)^{1/6} \sin\alpha_0^{-2/3} \hat{E}_0 Ai(\xi/l) \tag{48a}$$

$$E_{0,\perp} = 0 , \tag{48b}$$

where L is the scale height defined as $dX/dz|_{X=1} = 1/L$, $Ai(v)$ is the Airy function of argument v (Abramowitz and Stegun, 1970), and $l = (c^2 L \sin^2\alpha_0/\omega_0^2)^{1/3}$. Equation (48) is based on an approximation $N^2 \simeq (1-X)/\sin^2\alpha_0$, valid in the immediate neighbourhood of $X = 1$. A computed example is shown in Fig. 6, based on parameters of the experiment of Rietveld et al. (2000). From Eq. (48),

$$\max E_{0,\parallel} = K_{\mathrm{Ai}} \hat{E}_0 , \tag{49}$$

where the swelling factor for Airy maximum is given as

$$K_{\mathrm{Ai}} = 2\sqrt{2\pi} \left(\frac{\omega}{c} L \right)^{1/6} \sin\alpha_0^{-2/3} \max \mathrm{Ai} , \tag{50}$$

where the maximum value of the Airy function is $\max \mathrm{Ai} = 0.536$ attained at $\xi/l = -1.0$ (Abramowitz and Stegun, 1970). This gives the value

$$\Omega_{\mathrm{Ai}} = \frac{3}{4\eta} \frac{M}{m} \left(\frac{\omega_0}{c} \frac{L}{\sin\alpha_0} \right)^{-2/3} \tag{51}$$

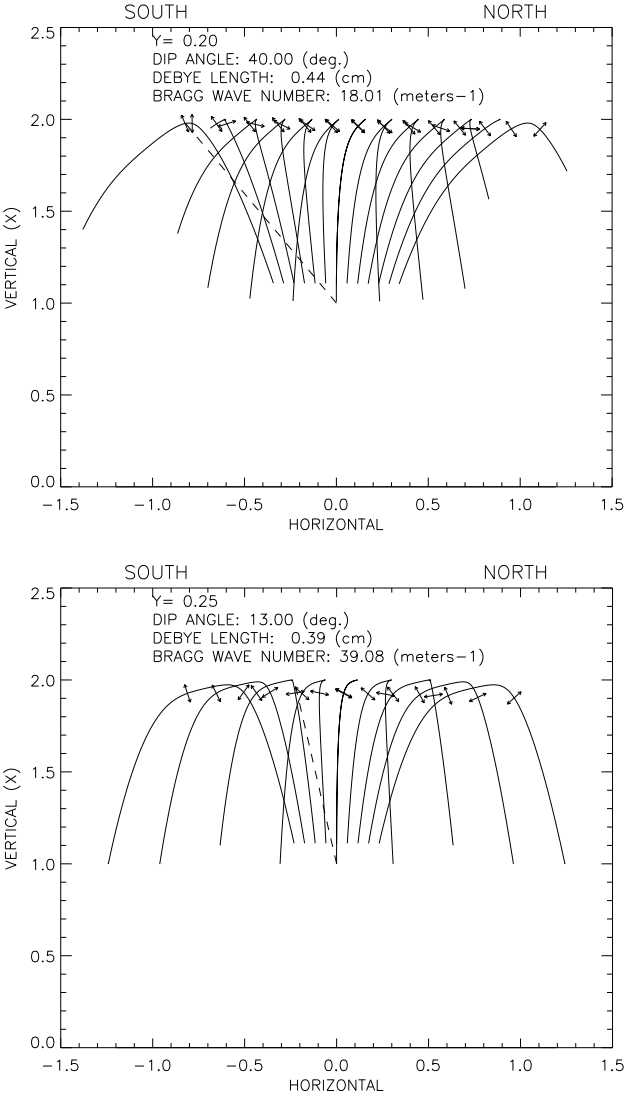

Fig. 7. Some examples of rays above HF transmitter, with polarization (of $\mathbf{E}_0$ component in the magnetic meridian plane) at matching height indicated by arrows. The ray tracing model underlying this, as well as Figs. 8 and 10, is briefly sketched in the main text, where the horizontal and vertical length scales are also explained. **(a)** A case corresponding to the Arecibo setup: dip angle 40°, $Y = 0.2$, based on $f_{ce} = 1.05$ MHz, Bragg wave number 18.01 m^{-1}, $T_e = 0.12$ eV (for calculation of matching height). **(b)** A case corresponding to the EISCAT UHF setup: $Y = 0.25$ (based on $f_{ce} = 1.35$ MHz), dip angle 12°, Bragg wave number 39.08 m^{-1}, $T_e = 0.1$ eV.

for Ω at Airy maximum. At the end of this section, Airy swelling at oblique incidence is briefly discussed. Alternatively, the uniform approximation of Lundborg and Thidé (1986) could have been used.

For the case of Fig. 6, quite extreme values of the electric field amplitude were obtained from our reference model at EISCAT VHF matching height and Airy maximum, respectively: $2K_\parallel = 9.6$ at matching height and $K_{\mathrm{Ai}} = 38.12$. For 240 MW ERP and $H = 245$ km, the reference field is

$\hat{E}_0 = 0.346\,\mathrm{V/m}$, which gives $E_{0,\parallel} = 3.3\,\mathrm{V/m}$ at matching height and $E_{0,\parallel} = 13.2\,\mathrm{V/m}$ at Airy maximum. For the parameters of Fig. 6, we have $\hat{E}_c = 0.94\,\mathrm{V/m}$, giving dimensionless values $E_{0,\parallel} = 3.5$ (matching height) and $E_{0,\parallel} = 14.0$ (Airy maximum). These are rather extreme values, compared to those that have been used in numerical solutions of the model (6) or its one-dimensional version. Extreme values were also noted by Lundborg and Thidé (1986) (cf. p. 493), and Djuth et al. (2002). For comparison, applying the same model to an Arecibo case ($\alpha_0 = 40°$, $f_{ce} = 1.05\,\mathrm{MHz}$, $f_0 = 5\,\mathrm{MHz}$, $L = 50\,\mathrm{km}$, $Q = 80\,\mathrm{MW}$ (ERP), $H = 245\,\mathrm{km}$, $T_e = 0.12\,\mathrm{eV}$), $E_{0,\parallel} = 1.3\,\mathrm{V/m}$ at matching height (dimensionless: 1.5) and $E_{0,\parallel} = 3.0\,\mathrm{V/m}$ (dimensionless: 3.5) at Airy maximum were obtained. Although far more moderate, still these values are large compared to those that have been used previously in theoretical work based on the model (6).

For the case of oblique incidence, the direction of the wave vector, i.e. the angle θ, must be determined by solving the Booker quartic (Budden, 1985) for N_ξ. We have developed a ray tracing model by simply considering the Booker quartic as a Hamiltonian and thus, following its O-mode root. Some results of this have been shown in Figs. 7 and 8. In our simplified model, we assume a vacuum up to 100 km, then a linear density profile with $L = 100\,\mathrm{km}$ up to the critical level $X = 1$, thus, interpreting the units on the axes of Figs. 7, 8, and 10 as 100 km.

In Fig. 7a, we show 13 rays, ranging from angles of incidence 18° to the south to 18° to the north, for a case corresponding to the Arecibo setup. The magnetic field direction is shown by means of a dashed line. The polarization at matching density is shown by means of arrows. For the central vertically incident ray, the polarization is seen to be essentially parallel to the magnetic field, thus, making an angle of $\sim 40°$ with the line of sight. On the other hand, for the southernmost rays, it is seen that the polarization in the downleg is more favourable. Figure 7b shows a similar picture for the Tromsø UHF case (9 rays with incidence from 12° south to 12° north). For the central ray (vertical incidence), one sees that the polarization at matching height is indeed very unfavourable. Again, the most favourable cases are the downward moving rays to the south. In Kohl et al. (1987) it is stated that, by experience, a "useful" configuration for plasma line observation with EISCAT UHF is to tilt the heater beam 6° to the south and observe along the magnetic field. We shall refer to this as the "Kohl setup". This corresponds approximately to the second ray towards the south counted from the central (vertical incident) ray. For the central, vertically incident ray, the polarization at VHF matching height is nearly along the magnetic field. Usually, in Heating-EISCAT VHF experiments, both the Heater and the VHF antenna are oriented vertically.

Let us elaborate a little further on the configuration based on the downward moving wave in the EISCAT UHF case. In Fig. 8a, b we show single rays at vertical incidence, 5.5° (a) or 6.75° (b) to the south. It is seen that the rays make a

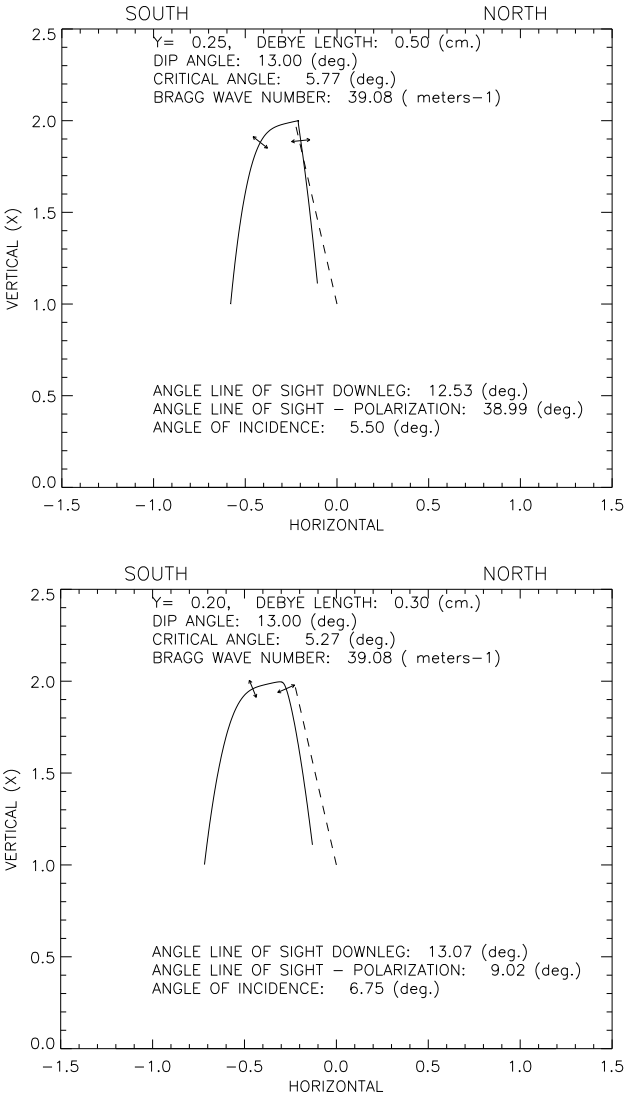

Fig. 8. Single rays to further illustrate the dependence of the polarization of the pump field at EISCAT UHF matching height on plasma parameters. **(a)** $Y = 0.25$; Debye length $\lambda_D = 0.5$ cm (corresponding to applied frequency $f_0 = 5.4\,\mathrm{MHz}$ and $T_e = 0.16\,\mathrm{eV}$). **(b)** $Y = 0.2$; $\lambda_D = 0.3$ cm (corresponding to applied frequency $f_0 = 6.75\,\mathrm{MHz}$ and $T_e = 0.09\,\mathrm{eV}$).

sudden change in direction on their downleg. If the matching height is hit above, or in the early stage of this change, a quite favourable configuration is obtained. For example, in Fig. 8b, an angle of 9° between $\mathbf{E}_0$ and the line of sight resulted. On the other hand, when the matching height is hit below or in the late stage, a far less favourable configuration results. In the example of Fig. 8a, the angle is 39°. The decisive ionospheric parameter determining the matching height is the Debye length: low temperature or high plasma density moves the matching height relative to the critical level upwards, according to Eq. (35). Increased density implies increased applied frequency ω_0, also decreasing the second term of Eq. (35). However, it was also found from studying the rays that reducing Y changes the ray in a way that coun-

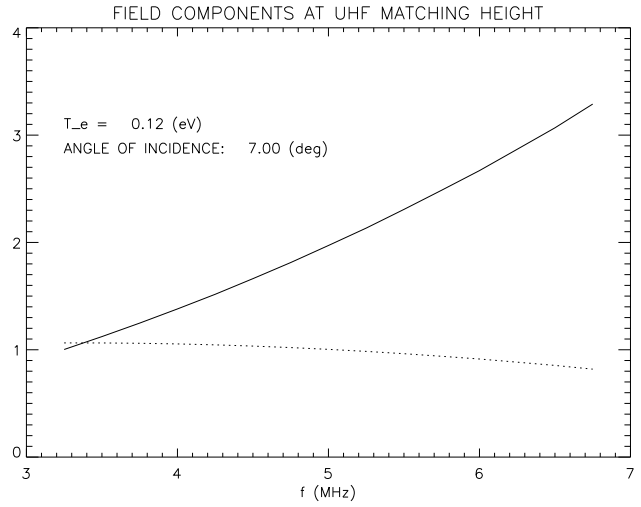

Fig. 9. Solid line: $K_{\parallel}$, broken line: $K_{\perp}$, at EISCAT UHF matching height on downleg, as a function of the applied frequency.

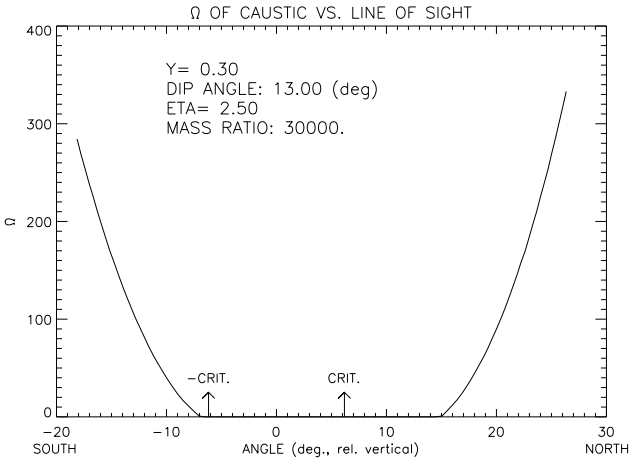

Fig. 11. The mismatch parameter Ω at the turning point as a function of the angle between the direction of the line of sight towards the turning point and the vertical. The markers indicate the spitze.

teracts this effect. In Fig. 9, this effect is illustrated quantitatively.

It is tempting to refer to the experimental work of Westman et al. (1995) in this connection: by changing the applied frequency from 5.423 MHz to 6.77 MHz, a plasma line spectrum was obtained with the monostatic UHF configuration with unprecedented detail: decay line and 5 cascades could be counted. The configuration corresponds by far to the one modelled in Fig. 8a: $\lambda_D = 3\,\mathrm{mm}$, $Y = 0.2$ which with $f_{ce} = 1.35\,\mathrm{MHz}$ corresponds to $f_0 = 6.75\,\mathrm{MHz}$; moreover, the angle of incidence of 6° and direction of sight of 12° also corresponds to the experiment.

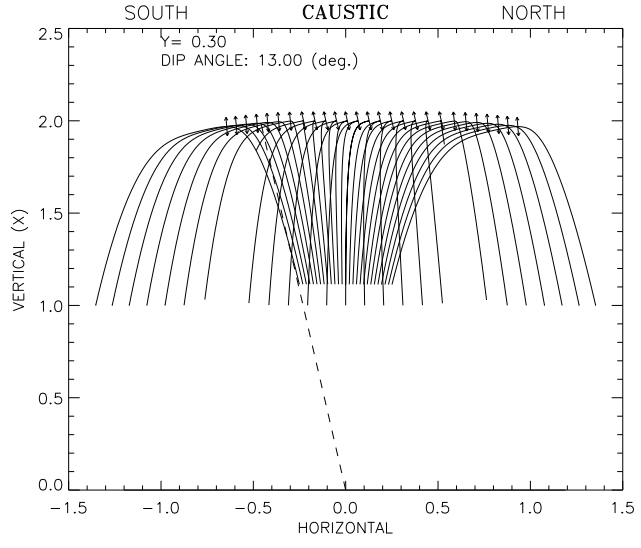

Fig. 10. The caustic of the ray bundle for Tromsø parameters. The arrows show the polarization of the electric field component in the magnetic meridian plane at the turning point.

It is well-known that the Tromsø UHF plasma line is difficult to observe in the range of larger Debye lengths, e.g. high temperature and low applied frequency. This has usually been attributed to an increased Landau damping, which increases the threshold (Stubbe et al., 1985). The feature illustrated in Fig. 8a, b offers an alternative explanation to this observation.

We have compared the Landau and collisional damping rates in the actual parameter range. Details are omitted. We concluded, as did Stubbe et al. (1985), that the Landau damping explanation is also feasible. The polarization feature described above represents an added effect.

Recently, there has been a de-emphasis of the role of the matching height for these oblique HF-UHF experiments and an increased emphasis on explanations in terms of cavitation (Isham et al., 1999b). For the Kohl setup (with the UHF radar pointing along the magnetic field), the HF wave field will not reach the critical level $X = 1$ on the radar line of sight, according to our horizontally stratified model. We shall call the highest point of a given ray (specified by its angle of incidence $N_\eta = \sin\theta_0$ and the plasma parameters) its turning point; other names may also exist. Thus, it has become of interest to discuss the possibility of explaining UHF observations as due to cavitating Langmuir turbulence near the turning point at oblique incidence. In the following, we report briefly on a study of what the input parameters to model (6) will be near the turning point, in particular, as seen at the line of sight 13° south.

Figure 10 shows an example of the rays over the HF transmitter above Ramfjordmoen, Tromsø, and the accompanying polarization of the electric field component in the magnetic meridian plane at the locus of the turning point. It is seen that inside the spitze range, where the wave reaches the critical level, the polarization is along the magnetic field, but outside of the spitze the polarization approaches vertical. In Fig. 11, we show an example of the calculated value of the

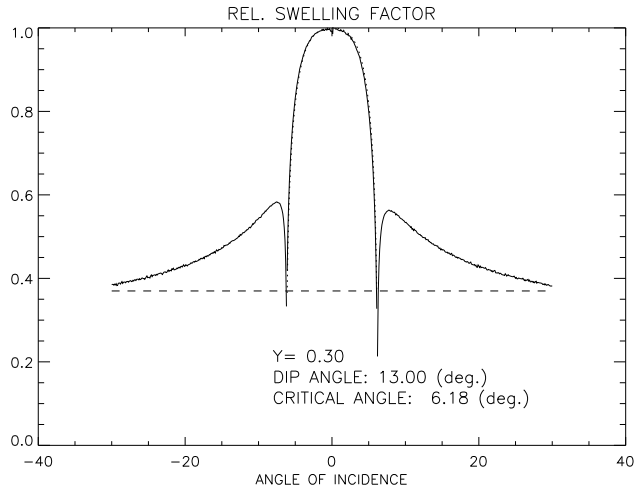

Fig. 12. The swelling factor as a function of angle of incidence, relative to that of normal incidence (as given by Eq. (50)). The broken line indicates $(\sin\alpha_0)^{2/3}$ with $\alpha_0 = 13°$, corresponding to the unmagnetized case.

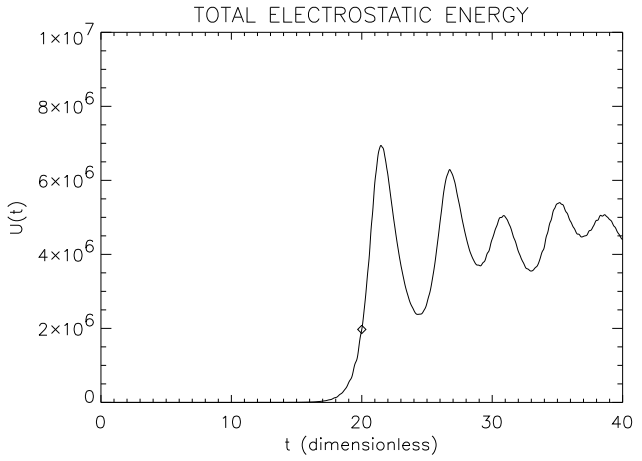

Fig. 13. Time evolution of U (Eq. (52)) for example I. Onset of averaging marked.

mismatch parameter Ω at the turning point, as a function of the angle between the vertical and the line of sight. It is seen that the value of Ω at the turning point seen at 13° south in the chosen example is around 100, i.e. as a rule-of-thumb, comparable with the value at VHF matching height.

Near the turning point, there will also be a swelling of the electric field amplitude, as in the case of vertical incidence described above. It should be stated that the relevant concept here is the caustic rather than the turning point, where the caustic is the envelope of the rays. We choose to replace the caustic by the turning point, which we expect to be a good approximation. The turning point will be the caustic for parallel rays, i.e. fixed N_η for all rays. Then the electric field in the vicinity of the turning point will be described by an Airy function of the vertical coordinate, in addition to the polarization relations at the turning point. The appropriate theoretical formulation of this for the case of oblique incidence does not exist in published form, according to the authors' present knowledge. In particular, at normal incidence, the factor $\sin\alpha^{-2/3}$ occurs in the swelling factor, which gives a strong extra swelling effect at high-latitudes. It is of interest to find out how this swelling effect behaves at oblique incidence. In Fig. 12, we show the swelling factor relative to that given by Eq. (50), as a function of angle of incidence. At the two critical directions, it formally goes to 0, however, near those values, the calculation is not valid anyway because coupling to the Z-mode takes place (Mjølhus, 1990). It is seen that for incidence around 10°, the swelling factor is still around half that of normal incidence. The details on the computations leading to Fig. 12 will be described elsewhere.

It is emphasized that the simple model described above should be considered as a reference model only. The two main sources of deviation are:

1. absorption,
2. refraction due to large-scale irregularities introducing horizontal gradients.

Both of them are essentially uncontrolled and unpredictable and it would, therefore, scarcely be of any help to try to implement them into the model. On the other hand, the electric field distribution in actual experiments must be expected to be influenced by these factors. For the absorption, there are two main components:

1. Absorption in the lower ionosphere (D layer), where the neutral density and consequently the collision frequency is high. This depends very strongly on the actual degree of ionization of these lower layers. It is also a question to what extent this ionization can be influenced by the high-power HF wave.
2. Anomalous absorption of the HF wave near the critical layer due to the energy loss into generation of the Langmuir turbulence, along the already traversed part of the ray path. For long duration high duty cycle exposure, one will also have strong anomalous absorption due to striations (e.g. Jones et al., 1984).

5 Some numerical examples

In this section, we show some selected examples of results of numerical solutions to Eqs. (6), in order to illustrate features discussed in Sects. 3 and 4, as well as to shed some theoretical light on recent experiments. The parameters of the examples are listed in Table 2.

The virtual radar power spectra that we show are calculated as described in the beginning of Sect. 4. We have normalized all the spectra by dividing them by the number of modes, $n_x \times n_y = 1024^2$. They are plotted against the dimensionless angular frequency ω, where in the plasma line

Table 2.

Example	I	II	III	IV	V
Ω	110	643	305	138	6
Ω_B	250	360	360	792	795
α	40°	52	0	10.6	0
E_0	1.1	1.51	1.0	1.2	1.8–2.0
ν	0.35	0.35	0.1	0.35	0.35
ν_{i0}	0.3	0.3	0.3	0.3	0.3
$L_x \times L_y$	54.83×54.80	$8\pi \times 8\pi$	$20\pi \times 20\pi$	$20\pi \times 20\pi$	$8\pi \times 8\pi$
δt	$5 * 10^{-4}$	$2.5 * 10^{-4}$	$1 * 10^{-4}$	$5 * 10^{-4}$	$2.5 * 10^{-5}$

channel the value $\omega = 0$ corresponds to no frequency shift relative to the applied frequency ω_0, and positive (negative) values of ω correspond to outshift (inshift). The frequency resolution is $\delta\omega = 2\pi/(N_1\delta t)$, where N_1 is the number of sampled values and δt is the time step.

Example I (Figs. 13–14) is intended to illustrate the geometric aspects of the maximum growth rates of the parametric instabilities, as discussed in Sect. 3 and illustrated in Fig. 4. In fact, the parameters of example I are the same as those of Fig. 4. In Fig. 13, we show the overall evolution by exhibiting the time evolution of the quadratic sum of all the Fourier modes

$$U(t) = \sum_{j_x=1}^{n_y} \sum_{j_y=1}^{n_x} |\mathbf{k}\Psi(k_{j_x}, k_{j_y}, t)|^2, \tag{52}$$

which is proportional to the total electrostatic energy of the simulation cell. One can see a growth stage, $0 \le t \le 20$ (in units (7)), and thereafter, in this case, damped modulations. In Fig. 14, we show contour plots of the time-averaged modal spectra, $\langle|\mathbf{k}\Psi(\mathbf{k}, t)|^2\rangle$, $\langle|n(\mathbf{k}, t)|^2\rangle$, where the averaging goes over $t_{\text{ave}} \le t \le t_{\text{end}}$, with $t_{\text{ave}} = 20$ and $t_{\text{end}} = 40$ in this case. In the upper panel, the direction of the driving electric field is indicated by an arrow ($\alpha = 40°$ in this case). The primary decay and two cascades can be seen. The excitation maximum in the **k**-plane is not along the driving electric field, but it agrees reasonably with the direction of maximum PDI growth rate of Fig. 4 (max excitation occurs in the range $20° < \theta < 25°$, while the theoretical max growth rate occurs at $\theta = 27°$).

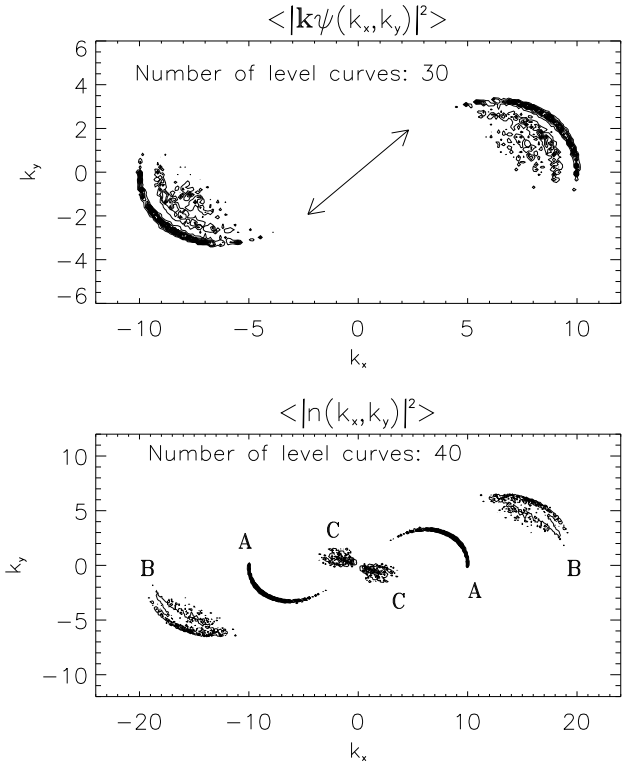

Fig. 14. Contour plots of time-averaged modal spectra, example I. Direction of driving electric field indicated with arrow in upper panel.

In the spectrum of n (lower panel), the primary decay (A) and the two first cascades (B) can also be seen; in addition, there is a spectrum in a range near $\mathbf{k} = \mathbf{0}$ (C) corresponding to density channels along the group velocity of the primary decay.

A feature of example I is that the OTSI has the overall largest growth rate. In addition, the system sizes L_x and L_y were chosen such that the **k** of maximum growth rate of the OTSI was approximated optimally in the numerical system. Still, the outcome of example I is saturation by cascade.

In Fig. 7b, the unfavourable polarization of the driving electric field at EISCAT UHF matching height at vertical radar line of sight is clearly exhibited. Nevertheless, Djuth et al. (1994) reported UHF observations in this experimental mode. Example II is devoted to a discussion of this situation. With $T_e = 0.15\,\text{eV}$ and $f_0 = 6.77\,\text{MHz}$, we have estimated the nondimensional probing wave number to $\bar{k}_p = 24.4$. With a line of sight of 13° to the magnetic field, this gives $\Omega \simeq 643$ at matching height. In the height-resolved observations of Djuth et al. (1994), the highest UHF observations occur about 1.5 km below the highest VHF spectrum, where the latter presumably came from the vicinity of the critical height. We have estimated the distance from the critical height down to the UHF matching height to 2.4 km, as-

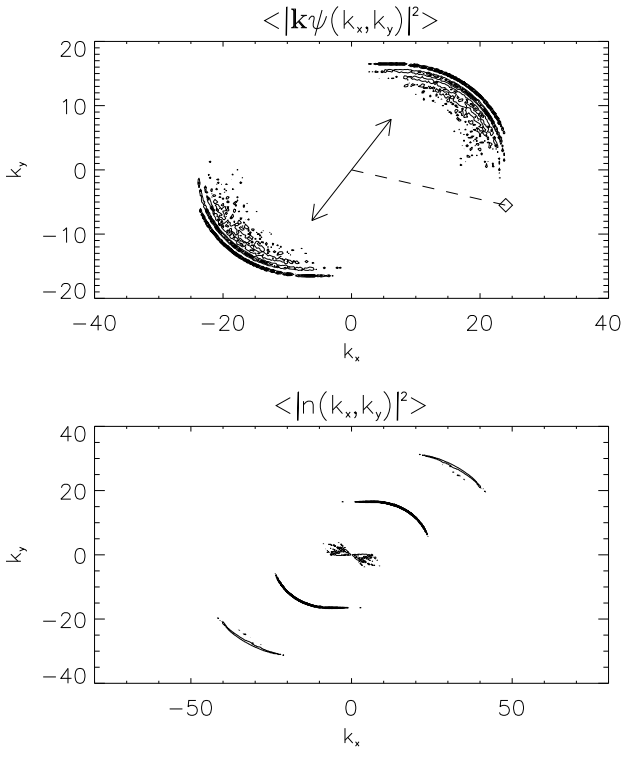

Fig. 15. Same as Figure 14, but for example II.

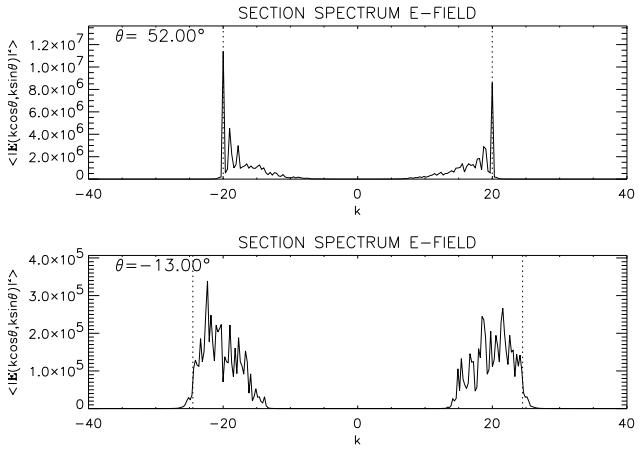

Fig. 16. Sections of the modal spectrum of **E** along the direction of $\mathbf{E}_0$ (upper) and along the radar probing direction (lower), example II. Locus of primary decay indicated by vertical dotted lines.

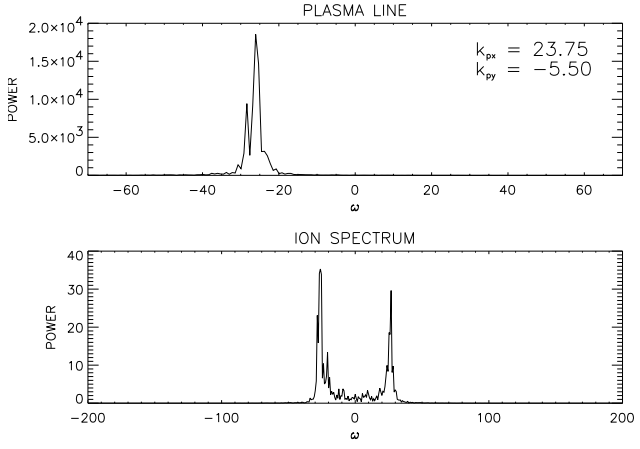

Fig. 17. Virtual radar spectra for example II. Five half-overlapping subspectra of length $N_1 = 2^{15}$, sampled with time step $\delta t = 2.5 * 10^{-4}$.

suming a scale height $L = 35\,\mathrm{km}$. We have calculated the polarization at the matching height to make an angle of 52° to the magnetic field. We chose a fairly large E_0 (= 1.51), corresponding to the "super heater" (1.2 GW ERP) used by Djuth et al. (1994). With gyrofrequency $f_{ce} = 1.35\,\mathrm{MHz}$, $\eta = 2.5$ and mass ratio $M/m = 3 * 10^4$, we have $\Omega_B = 360$.

Some results of example II are shown in Figs. 15–17. Figure 15 shows the modal spectra, averaged over $15 \le t \le 40$. In the upper panel, the electric field polarization and the virtual radar are indicated. One sees that this example again appears as cascade-saturated. Figure 16 shows sections of the modal spectrum of **E** along the two directions indicated in Fig. 15. The wave number of primary decay instability in the two directions, according to Eq. (21), are indicated. We see that along the radar direction, the maximum excitation is not at the primary decay. The excitation level along the radar direction is $\sim 1/30$ of that along the driver direction.

Figure 17 shows the virtual radar spectra for this situation. It will be interesting to compare them with virtual radar spectra of example V. In example II, we ran 9 nearby virtual radars. Surprisingly, the frequency downshift of the plasma line varied considerably in the range $-10 > \omega > -40$.

Also, the setup at Arecibo has been recognized as geometrically unfavourable, with the $\mathbf{E}_0$ polarization nearly along the magnetic field, and the radar line-of-sight usually along the vertical, making 40°–45° with $\mathbf{E}_0$, cf. Fig. 7a. This is discussed in detail in DuBois et al. (2001) and Cheung et al. (2001). In example III, we show a case pertaining to that situation. The parameters were chosen in order to represent the case of DuBois et al. (2001). In the latter, the values of the parameters were determined on the basis of an artificial low mass ratio of $M/m = 6200$, and the numerical representation of the system was with 256×256 Fourier modes. In example III, the parameters are estimated from the physical values given by DuBois et al. (2001) using mass ratio $M/m = 30\,000$, and the system is represented with 1024×1024 modes. DuBois et al. (2001) used the following data: electron temperature $T_e = 1000°\,\mathrm{K}$, applied frequency $f_0 = 5.1\,\mathrm{MHz}$, electron gyrofrequency $f_{ce} = 1.05\,\mathrm{MHz}$, line of sight 45° to magnetic field; from this, DuBois et al. (2001) estimated $X_{\mathrm{match}} = 0.962$ for the matching height. Moreover, DuBois et al. used $\eta = 3.383$ ("best fit 2-pole approximation" (DuBois et al., 1995)). Then, $\Omega = 253$, $\Omega_B = 266$ are obtained, and for the case of a driving electric field amplitude of 1 V/m, we obtained $E_0 = 1$. Finally,

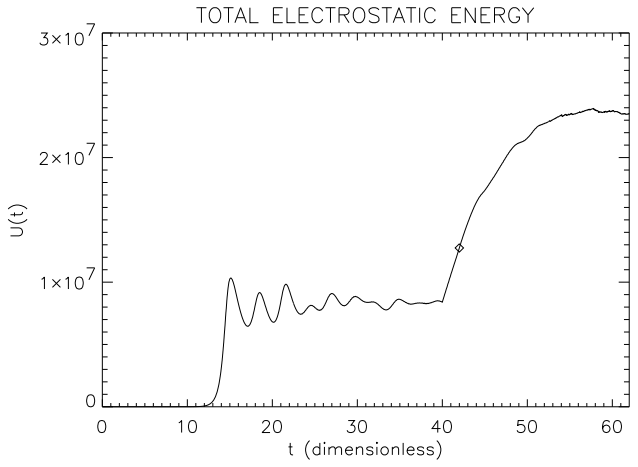

Fig. 18. Time evolution of U for example III. For $0 \le t \le 40$, it was run with $\nu = 0.25$, while for $40 \le t \le 62$, $\nu = 0.1$. Onset of averaging and virtual radar sampling at $t = 42$ marked.

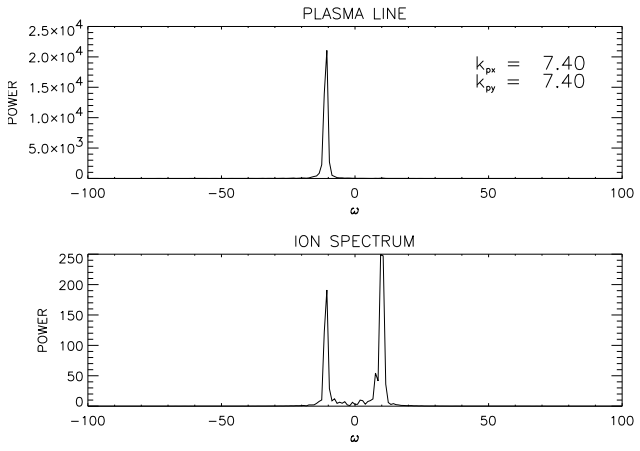

Fig. 20. Virtual radar spectra for example III. Three half-overlapping subspectra of length $N_1 = 2^{14}$, sampled with time step $\delta t = 10^{-4}$.

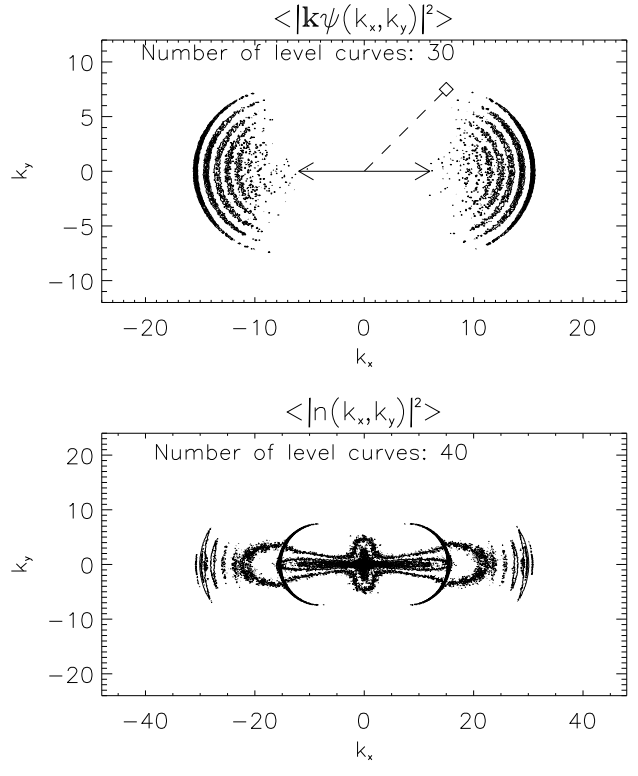

Fig. 19. Contour plots of time-averaged modal spectra for example III. Driver and virtual radar indicated in upper panel.

for the electron collision frequency, DuBois et al. state that $\nu_{ec}/\omega_{pe} = 1.5 * 10^{-5}$. From this we obtain $\nu = 0.1$. Finally, DuBois et al. put $\nu_{i0} = 0.32445$ (again, "best fit two-pole approximation").

The results for example III are shown in Figs. 18–20. The plasma line strength of Fig. 20 is about half that of Fig. 22 below, while the ion spectrum is about one-fifth of the latter. It is also interesting to compare with the results of Mjølhus et al. (2001), where radar matching of numerically generated Langmuir spectra was promoted by refraction in plasma density ducts. Both virtual radar spectra of Fig. 8 of Mjølhus et al. (2001) are about one-half of the corresponding spectra of Fig. 20.

As has been emphasized in many papers, the main prediction from the model (6) is saturation by decay-cascades at some distance below the O-mode reflection level, which will be observable by a radar detecting scattered signal from the radar's matching height Eq. (34), and a cavitating turbulence just below the reflection level, expected to be observable by a range of radars (Hanssen et al., 1992; DuBois et al., 1993a, b; 2001). This qualitative prediction has indeed been supported by experiments in great detail (Sulzer and Fejer, 1994; Rietveld et al., 2000; Cheung et al., 2001; Djuth et al., 2002). In particular, Rietveld et al. (2000) presented an example with height-separated spectra of cascade versus cavitation type obtained by the Tromsø VHF radar. In Sect. 4, we made estimates of the electric field strength and polarization for data corresponding to that experiment. In the next two examples, we show numerical results obtained for parameters chosen relative to the Rietveld et al. (2000) experiment.

Let us first emphasize that, by using electric field values as estimated in Sect. 4, or corrected for, say, 30% D-layer absorption, (i) model (6) cannot currently be handled numerically, and (ii) would be expected to lead to a prediction of cavitating Langmuir turbulence in all of the height ranges from which HF-enhanced backscatter was obtained by the EISCAT VHF radar in the Rietveld et al. (2000) experiment. In the examples we show, we have used far smaller values of E_0 than those estimated in Sect. 4.

In example IV, parameters corresponding to the matching height for the experiment of Rietveld et al. (2000) have been used: the line of sight of the virtual radars (we ran 15 altogether) made about $-13°$ to the magnetic field, correspond-

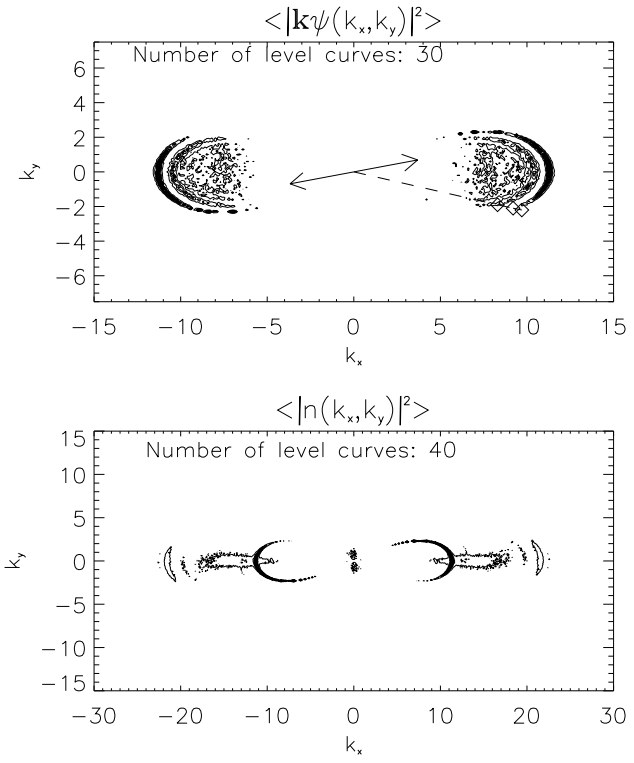

Fig. 21. Contour plots of modal spectra, example IV. Averaging and virtual radar sampling were done for $60 \le t \le 90$. Virtual radars (3) and driver indicated in upper panel.

ing to vertical probing. The component of the driving electric field in the magnetic meridian plane made 10.6° with the magnetic field. For the mass ratio, we used $M/m = 3 * 10^4$, we put $\eta = 2.5$, $f_0 = 4.54$ MHz and $f_{ce} = 1.35$ MHz; this gives $\Omega_B = 792$. Furthermore, we assumed $T_e = 2000°$ K, which gives a nondimensional probing wave number $\bar{k}_p = 9.4$; this, in turn, gives a matching height of $\Omega = 138$.

Some results of example IV are shown in Figs. 21–24. Figure 21 shows the modal spectra. In Fig. 22, we show the spectra for the virtual radar which comes closest to the matching for the primary decay line. It shows the decay line with the correct downshift (upper panel) and the ion shoulders with correct shift (lower panel). In addition to this, we show in Figs. 23 and 24 interesting results of two other virtual radars run in example IV. In Fig. 23, we show spectra corresponding to a virtual radar $\bar{\mathbf{k}}_p = (9.6, -2.2)$, which is near the growth range for the OTSI instability. In the plasma line spectrum, there is a sharp peak centered at vanishing frequency shift, about 1/10 of the intensity in Fig. 22, and similarly for the ion spectrum. Strangely, the wave number of this virtual radar is slightly below the OTSI growth range. It seems that it is necessary to use a value of the parameter ν_{i0} that is not too small, in order to observe these "OTSI" features in cascade cases (Sprague and Fejer, 1995). We also ran a virtual radar at $\bar{\mathbf{k}}_p = (9.7, -2.2)$, which is in the growth range of the OTSI. The spectra showed similar features, but at a lower intensity. In Fig. 24, we show the result of a virtual

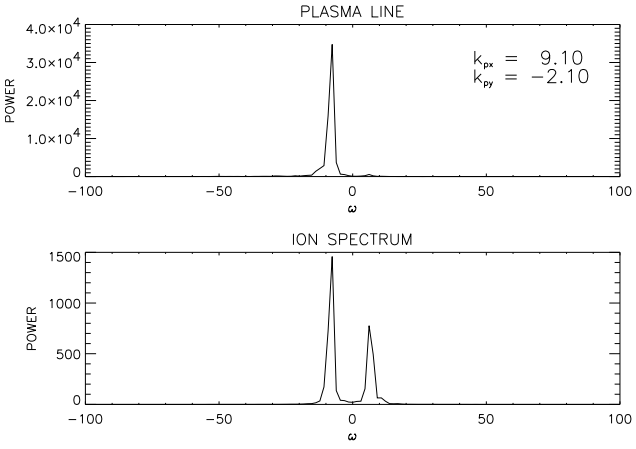

Fig. 22. Virtual radar for example IV. Sixteen half-overlapping spectra of length $N_1 = 2^{13}$, sampled with time step $\delta t = 5 * 10^{-4}$. In this figure: a radar resonant with the primary decay.

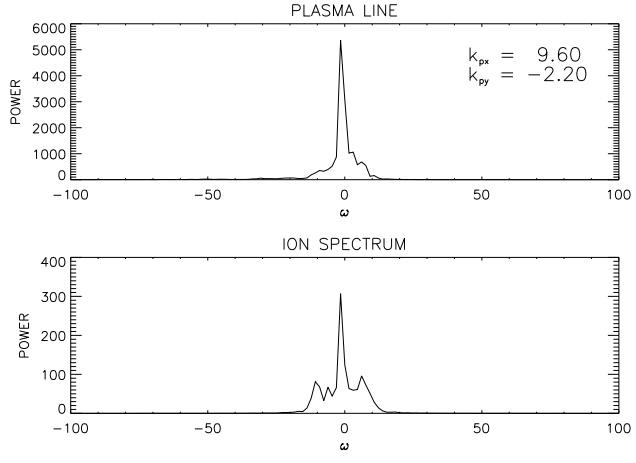

Fig. 23. Another virtual radar for example IV. Same sampling and averaging as in Fig. 22.

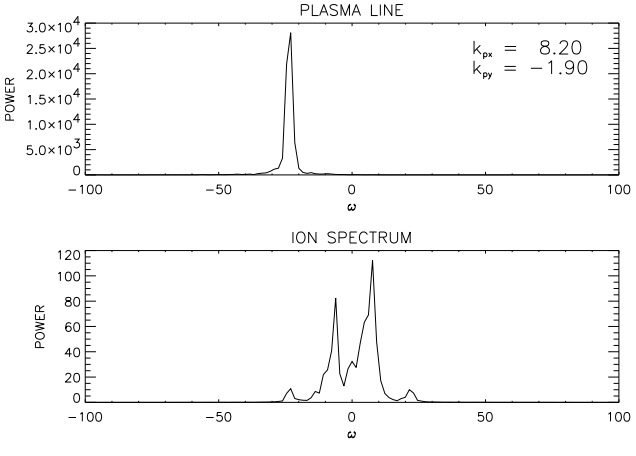

Fig. 24. Another virtual radar for example IV. Same sampling and averaging as in Fig. 22.

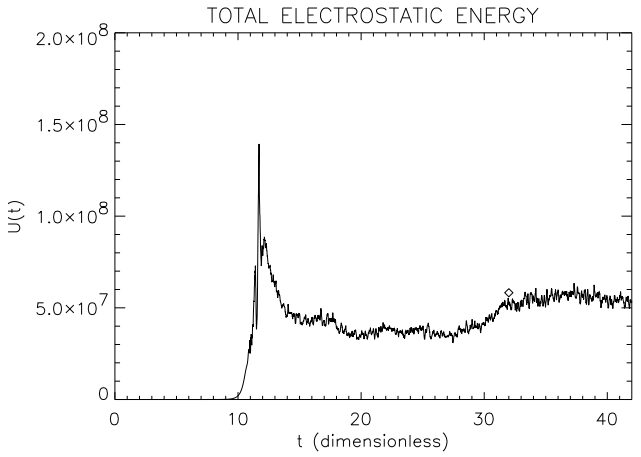

Fig. 25. Time evolution of U in example V. For $0 \le t \le 30$, $E_0 = 1.8$, while for $30 \le t \le 42$, $E_0 = 2.0$. Start of averaging and sampling at $t = 32$ marked.

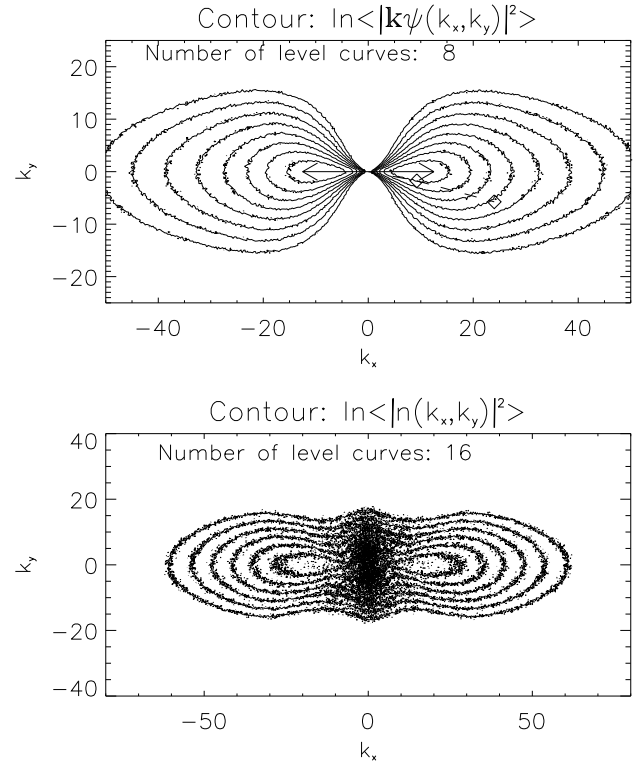

Fig. 26. Contour plots of the natural logarithm of the averaged modal spectra of example V. Contours of $\ln(A(\mathbf{k})/\max A)$ are plotted with equidistance equal to 0.5, and $A(\mathbf{k}) = \langle|\mathbf{k}\Psi(\mathbf{k})|^2\rangle$ or $\langle|n(\mathbf{k})|^2\rangle$. Averaging was done for $32 \le t \le 42$.

radar at $\bar{\mathbf{k}}_p = (8.2, -1.9)$. In this case, the plasma line virtual radar probes the first cascade, which comes out even stronger than the primary decay line of Fig. 22. In the ion spectrum, we see traces of the third harmonic reported by Kohl and Rietveld (1996).

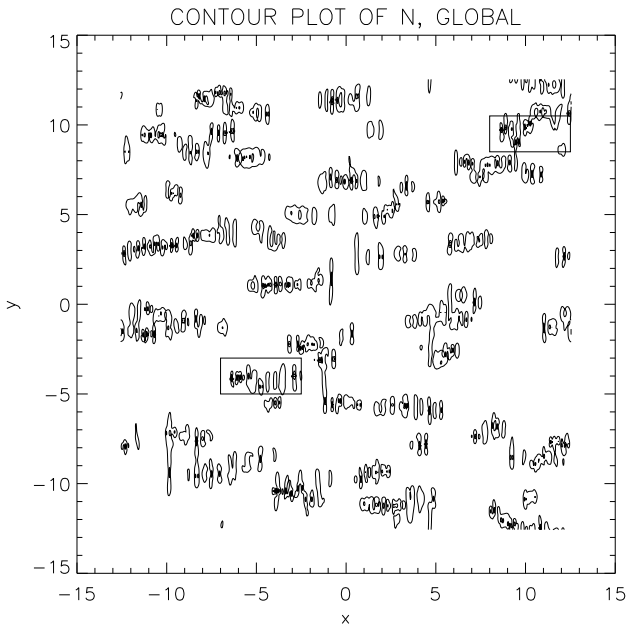

Fig. 27. Contour plot of the density at $t = 30$ for example V, whole spatial system. 20 levels. Cuts of Figures 28 and 29 shown.

In example V, parameters were intended to represent the conditions at the Airy maximum. Using parameters as in Fig. 6 and formula (51), we obtain the value $\Omega = 6$, and polarization along the magnetic field. However, according to the estimates in Sect. 4, the ratio between the electric field at Airy maximum and EISCAT VHF matching height should be about 4, so relative to example IV, we should use $E_0 = 4.8$. In example V, we use, for numerical reasons, the far smaller value $E_0 = 2.0$, polarized along the magnetic field. Actually, we ran $E_0 = 1.8$ for $0 \le t \le 30$, and $E_0 = 2.0$ for $30 \le t \le 42$. Even with these values, we had to use a time step as small as $\delta t = 2.5 * 10^{-5}$. With a larger time step, the numerics collapsed once cavitation started. We show some results in Figs. 25–31. Figure 25 shows the time evolution of U. In particular, we see the change at $t \ge 30$, where E_0 was increased. Figure 26 shows contour plots of the time-averaged modal spectra for $\nabla\Psi$ and n. In order to exhibit the full range of them, we had to plot equidistant contours of the logarithm. Clearly, this is in the cavitation range. Figure 27 shows a contour plot of n at $t_{\text{end}} = 30$ for the whole simulation cell $D = [-4\pi, 4\pi] \times [-4\pi, 4\pi]$. Figure 28 shows contour plots of $n(\mathbf{x}, t_{\text{end}})$ and $|\nabla\Psi(\mathbf{x}, t_{\text{end}})|^2$ in a smaller spatial cell near the minimum value of n, and Fig. 29 is similar for a spatial cell near the maximum value of $|\nabla\Psi|^2$. It should be noted that the extreme values of n and $|\nabla\Psi|^2$ of Figs. 28 and 29 break conditions (4), (5) for the validity of the model. Nevertheless, we choose to report this example, both in order to exhibit interesting qualitative features occurring in examples of cavitation with this large value of Ω_B, and also because such extreme values occur only occasionally within the end state of example V.

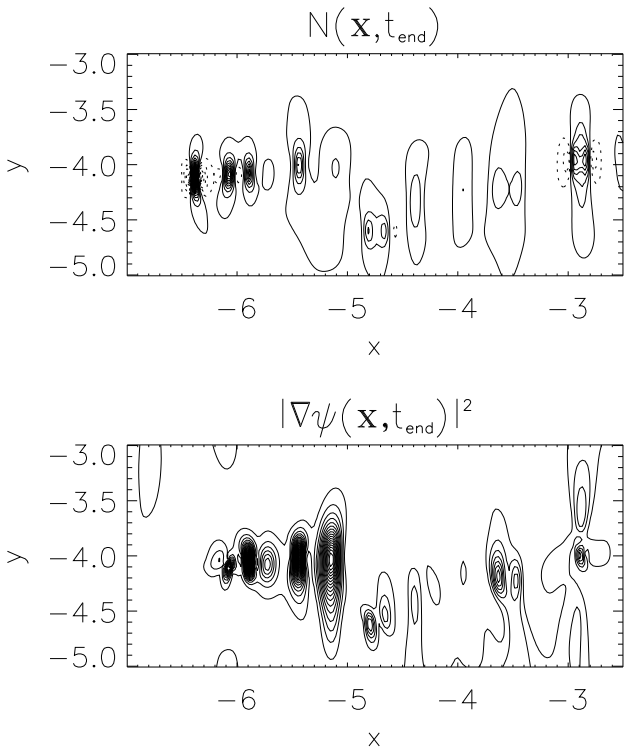

Fig. 28. Contour plots of density and ponderomotive pressure of the state at $t = 30$ of example V in a section of the spatial system containing the minimum point of n. Broken lines in the contour plot of n correspond to positive values of n. In each plot, 40 equidistant levels are used. The minimum value of n is $n_{\min} = -8874$, occurring at $(x, y) = (-6.38, -4.12)$; the maximum value is $n_{\max} = 2173$, occurring at $(x, y) = (-6.33, -4.12)$. The maximum value of $|\nabla\Psi|^2$ is 1465, occurring at $(-5.89, -4.05)$.

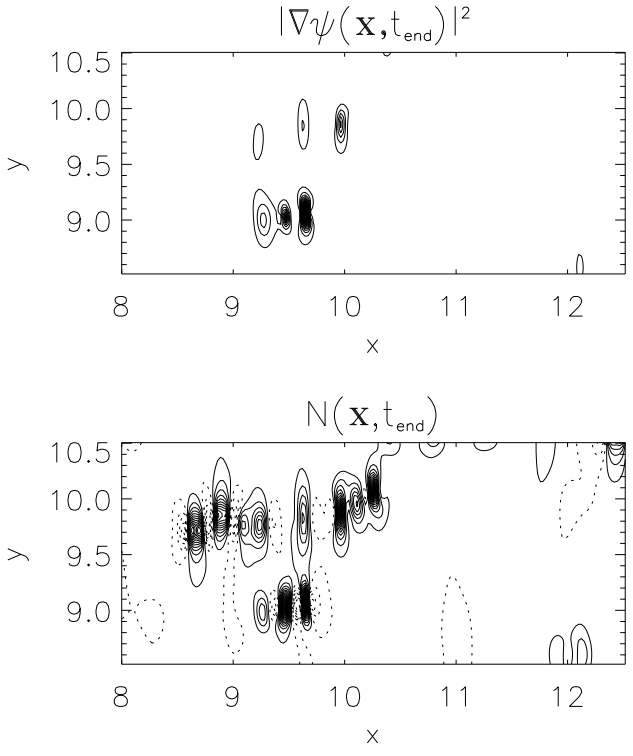

Fig. 29. Contour plots of ponderomotive pressure and density of example V at $t = 30$ in a section of the spatial system containing the maximum point of the ponderomotive pressure. Broken lines in the contour plot of n correspond to positive values of n. In each plot, 40 equidistant levels are used. The maximum value of $|\nabla\Psi|^2$ is 18561, occurring at $(x, y) = (9.6, 9.06)$. The minimum value of n is $n_{\min} = -3860$, occurring at $(x, y) = (9.65, 9.06)$, and the maximum value is 861, occurring at $(x, y) = (9.57, 9.06)$.

From Figs. 27–29, the following properties are observed: (i) the cavitations are strongly anisotropic, with a short length scale along $\mathbf{B}_0$ and a much longer scale transverse to $\mathbf{B}_0$. This is a result of the large value of the magnetic parameter Ω_B, so the shape expresses a balance between the parallel derivative contribution to the last term, and the next to the last term, of the left-hand side of Eq. (6a):

$$\frac{\partial^4\Psi}{\partial x^4} \quad \text{versus} \quad \Omega_B \nabla_\perp^2 \Psi \,.$$

For the undriven case, this feature was discussed by Petviashvili (1975) and Krasnoselskikh and Sotnikov (1977); (ii) a further consequence of this anisotropy, is that there is a clear up-stowing of plasma at each side of the cavities, along the magnetic field direction. This can be seen in Figure 28 as broken level curves (corresponding to positive density perturbations), e.g. at each side of the cavity positioned at $(-6.38, -4.12)$; similar features can be seen around all of the stronger cavities in Figs. 28 and 29. The crudest picture of trapping of Langmuir oscillations requires that the caviton is surrounded by states with $\Omega_\theta - n < 0$, where Ω_θ is defined in Eq. (16b), and θ is measured as the angle between the magnetic field direction and the direction of the line from the center of the cavity to the actual point. This condition expresses that Langmuir waves at the applied frequency ω_0 cannot escape from the cavity in any direction. From this consideration, it follows that this anisotropic up-stow promotes trapping, because n is positive where Ω_θ is largest. Therefore, it is inferred that the anisotropy of large Ω_B promotes cavitation. Essentially, the large value of Ω_B makes the process more similar to the one-dimensional situation studied in Hanssen et al. (1992); (iii) one sees from Figs. 28 and 29 that there is not a complete correlation between density depressions and strong localized peaks in $|\nabla\Psi|^2$. For example, for the strong caviton seen in Fig. 28 around position $(x, y) = (-6.38, -4.12)$, there is no visible accompanying ponderomotive peak. Apparently, the electric field of this caviton is burnt out (DuBois et al., 1990). On the other hand, there appear several cavitons to the right of this, with accompanying ponderomotive peaks. This is consistent with the dynamical picture of the cavitation process, which is appropriate for the driven model (6), consisting of an initial local cavity resonance in a density depletion leading to a rapid growth of a localized electric field ("nucleation"), subsequent

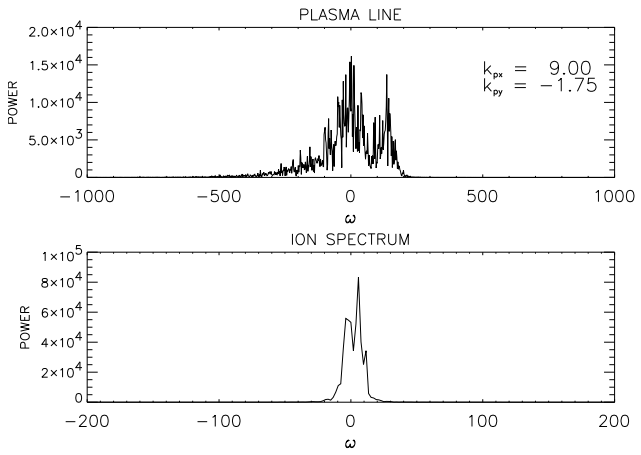

Fig. 30. Virtual radar spectra of example V at $\bar{\mathbf{k}}_p = (9.0,\ -1.75)$. Eight half-overlapping subspectra of length $N_1 = 2^{17}$ sampled at time intervals $\delta t = 2.5 * 10^{-5}$.

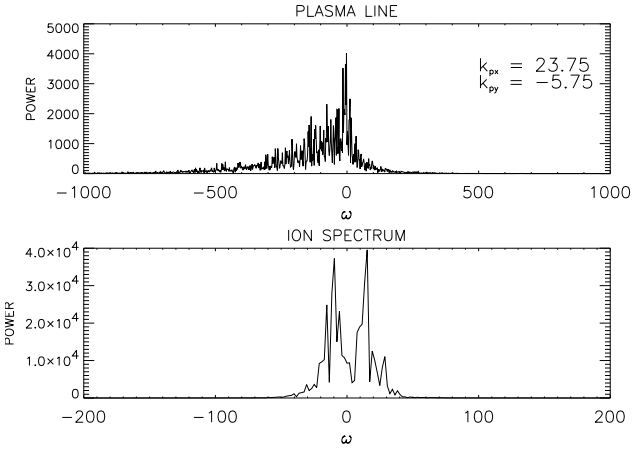

Fig. 31. Virtual radar spectra of example V at $\bar{\mathbf{k}}_p = (23.75,\ -5.75)$ sampled and averaged as in Fig. 30.

inertial collapse, burn-out, and re-nucleation (DuBois et al., 1990); (iv) an interesting observation, for which we presently have no explanation, is that the cavitations appear to occur in groups or strings, aligned along the magnetic field. This is seen in all of Figs. 27–29. This observation underlines the quasi one-dimensional character of cavitation at these large values of Ω_B.

In Figs. 30 and 31, we show power spectra for two virtual radars. In Fig. 30, the probing wave vector is similar to that of Fig. 22, i.e. corresponding to the EISCAT VHF observations of Rietveld et al. (2000), while in Fig. 31, the probing wave vector is similar to that of Fig. 17, i.e. the EISCAT UHF observations of Djuth et al. (1994). The two values of $\bar{k}_p$ are not in the ratio of the Bragg wave numbers of the EISCAT UHF and VHF, due to different physical parameters in the two experiments. Figure 30 shows a pronounced outshifted feature (a "free mode" (DuBois et al., 1988, 1990)). Such features are not seen in the VHF data of Kohl and Rietveld (1996) or Rietveld et al. (2000), but occur pronounced in the results obtained by Djuth et al. (2002). The power of the plasma line of Fig. 30 is about one-half of that of Fig. 22, while the ion spectrum of Fig. 30 is ~ 60 times stronger than that of Fig. 22. Trends of this nature are pronounced in the data of Rietveld et al. (2000). The width of the plasma line spectrum of Fig. 30 is of the order of 20–30 times the downshift of the decay line of Fig. 22. Something similar appears to be the case comparing the "cavitation" and "cascade" type spectra of Rietveld et al. (2000) (e.g. Fig. 2).

The plasma line of Fig. 31, taken at a virtual radar similar to that used in Fig. 17 (example II), is about 1/5 that of Fig. 17; the strongest plasma line obtained by the various virtual radars run in example II was about ten times stronger than that of Fig. 31. On the other hand, the ion spectrum of example II (Fig. 17) is $\sim$ 100–200 times weaker than the corresponding one in example V (Fig. 31).

In Isham et al. (1999b), strong outshifted features ("free mode") were observed in spectra taken by the EISCAT UHF. Such a feature is not seen in Fig. 31, but could be seen for $14 \le t \le 30$ ($E_0 = 1.8$), with $\bar{k}_p = 20$, making angle $-13°$ to the magnetic field.

6 Discussion

One may say that "a good qualitative understanding of the first 10 milliseconds" of the Arecibo experiments has been obtained, first through the experimental reports of Cheung et al. (1989, 1992), Fejer et al. (1991) and Sulzer and Fejer (1994), and their relation to theory (DuBois et al., 1988, 1990, 1993a, b; Hanssen et al., 1992) and then in even greater detail and precision by the twin papers by DuBois et al. (2001) and Cheung et al. (2001). The height-resolved radar observations in these experiments are in qualitative agreement with the predictions obtained from the local model (6) when Ω is interpreted as proportional to the vertical distance below the critical height. For a detailed discussion of this, we refer to DuBois et al. (2001) and Cheung et al. (2001).

In order to interpret the parameter Ω as relative height, a slowly varying horizontal stratification is presumed. On a longer time scale, the strong HF exposure is supposed to lead to local plasma density inhomogeneities due to various sources; as a consequence, one loses the simplicity of the interface between the local processes and the radar observations. The present authors hold the view that the success of "the first 10 ms" leads to a confidence in the theoretical understanding of the local process, and that explanations of the long time development of observations should be most of all sought in the development of the interface between local processes and radar observations, due to inhomogeneities. The paper (Mjølhus et al., 2001) attempts to contribute in this direction. In addition, modification of the electron distribution function may also have to be taken into account for a longer time scale understanding.

While the Arecibo experiments have received extensive theoretical attention, there has also been an extensive number of reports of experimental work from the EISCAT facilities, starting with Hagfors et al. (1983). In the present paper, an attempt is made to emphasize the comparison of theory and experiment for these experiments.

As discussed in Sect. 4, there is a great variety of modes by which the Tromsø experiments can be performed or theoretically interpreted. This makes it complicated to focus attention and decide whether the bulk of the experiments "agree" or "do not agree" with the current theory. In the following, we shall comment on a few of the most recent experimental reports.

For the EISCAT VHF experiments, the papers by Rietveld et al. (2000) and Djuth et al. (2002) present some of the most well-resolved Tromsø results to date. Spectra in height bins of 300 m resolution were presented. For the Rietveld et al. (2000) experiment, due to an unusually small density gradient (estimated scale height $L \sim 160$ km) and a stably smooth ionospheric plasma state, height-separated spectra of clearly different types were presented, with spectra resembling those predicted theoretically in cases of cavitation in the upper height bins, and line structured spectra representative of cascade in the lower height bins, and in between, there were in some cases height bins with no detectable HF-induced spectra. A situation with height-separated spectra of different types was shown to have been maintained over some tens of minutes during the experiments (0.4 s on, 9.6 s off). The ion spectra from those upper height bins, in particular, showed a resemblance to numerical calculations presented in Hanssen et al. (1992), for example, the lower panel of Fig. 25. It is our experience from a large number of calculated virtual radar ion spectra from cavitating Langmuir turbulence, that they can vary quite a lot in appearance. This also appears to be the case in the spectra presented in Djuth et al. (1994), Kohl and Rietveld (1996), Rietveld et al. (2000), and Djuth et al. (2002). We also refer to a discussion by Hanssen (1992) of the significance of integration time.

The virtual radar plasma line spectrum in the upper panel of Fig. 30 shows a pronounced outshifted feature (a "free mode"). No such feature is seen in the spectra of Rietveld et al. (2000). This may be due to the bandwidth used (50 kHz), or a duty cycle that is too high. In Djuth et al. (2002), where the experiment was performed at an extremely low duty cycle in order to maintain controlled conditions, such outshifted features occur in the "cavitation type" spectra in the upper height bins, but not in line-structured spectra in the lower height bins, as predicted. An example of a VHF spectrum with an outshifted feature also occurs in Fig. 10 of Kohl et al. (1993).

For numerical reasons, we ran the values $E_0 = E_m = 1.2$ at VHF matching height (example IV) and $E_0 = E_{\mathrm{Ai}} = 2.0$ at Airy maximum (example V), while the estimates using the model of Sect. 4 led to nondimensional values $E_0 = E_{0m} = 3.5$ at matching height and $E_0 = E_{0\mathrm{Ai}} = 14$ at Airy maximum. Using a simple absorption model, we have estimated that the numerical values E_m and E_{Ai} are consistent with 57% absorption before VHF matching height and further 95% absorption from VHF matching height to Airy maximum. We omit details on this, but it should be noted that the hypothetical strong absorption in the upper layer implies that the reflected wave at VHF matching height is absent, thus, alone accounting for a halving of the electric field strength at VHF matching height.

We cannot say to what extent the values E_m and E_{Ai} used in examples IV and V are unrealistic. Ninety-five percent absorption in the short path from VHF matching height to Airy maximum appears extreme. For the total absorption of the pump wave due to ponderomotive Langmuir turbulence over all its height range, we have measurements such as those reported in Fejer and Kopka (1981), or Frolov et al. (1997; and references therein). In the latter, a total absorption of $\sim$80% is reported at 60 MW ERP at the Sura facility, Russia, and less at lower incident power. We have run a case with $E_m = 1.8$ and otherwise parameters as in example IV; then the dynamics went to cavitation. Thus, with this (nondimensional) electric field strength at VHF matching height, cavitation is expected in the full height range observed by the VHF radar in the experiment of Rietveld et al. (2000). In the experiments by Djuth et al. (1994), the full power of the "Tromsø superheater" was used (1.2 GW ERP). In this case, it may seem that the VHF spectra are of the cavitation type in all height bins. In the results presented by Kohl and Rietveld (1996) (Figs. 1 and 2), a similar ERP was used; in that case, there is a continuous transition from cascade-like to cavitation-like spectra.

Recently, the experimental report of Djuth et al. (2002) of EISCAT VHF measurements has become available. The results show many similarities with those of Rietveld et al. (2000), although the methods for obtaining high spatial resolution are very different. Djuth et al. (2002) used an even lower duty cycle (0.1 s on, 29.9 s off) than Rietveld et al. (2000), in order to eliminate memory effects. Djuth et al. (2002) do not report examples where there is a height interval between spectra of the cavitation versus cascade type. Also, outshifted features with frequency shifts compatible with the dispersion relation, generally occurred in the cavitation type spectra, such as the "free mode" of Arecibo experiments. Djuth et al. (2002) also present extensive measurements of decay rates after HF turn-off, of the various spectral features. They were generally considerably higher than those expected from linear damping rates. This obviously presents us with new theoretical challenges. Finally, it contains a useful experimental estimate of the D-layer absorption during the experiment. Since the report by Djuth et al. (2002) has become available only after the bulk of the present work was completed, we cannot enter an extensive comparison of our work with those results, and none of our presented examples I-V of Sect. 5 were designed for comparison with Djuth et al. (2002).

We conclude that the EISCAT VHF observations are in qualitative agreement with predictions from the model (6). Quantitatively, we cannot say too much, because we cannot handle numerically as large an electric field as estimated in

Sect. 4, and we do not know the absorption. What we can say is that with low absorption (say, 30% up to VHF matching height and $< 10\%$ further up to Airy maximum), cavitation is expected for all heights for the VHF radar, in the case of the Rietveld et al. (2000) and Djuth et al. (2002) experiments.

Turning to EISCAT UHF observations, the picture appears even more bewildering. In Sect. 4, we presented some studies of the electric field polarization at UHF matching height for various angles of incidence. The polarization in the case of vertical incidence is rather unfavourable for observable cascading. In the height-resolved experiment of Djuth et al. (1994), the HF transmission was either vertical or directed 5° south. In either case, plasma line and ion spectra were detected, in spite of the expectedly unfavourable geometry. The UHF spectra occurred from a height range that was lower than, but overlapped with, the height range of the VHF spectra. From theoretical grounds, one would expect cavitation spectra from the largest height: the same as the largest heights from which VHF spectra were obtained; these heights one would expect to coincide with the Airy maximum for the pump wave. That, however, is not the case in the UHF observations of Djuth et al. (1994). An estimation of distance from the critical height down to the UHF matching height, based on scale height $L = 35\,\mathrm{km}$, electron temperature $T_e = 0.15\,\mathrm{eV}$, and frequency $f_0 = 6.77\,\mathrm{MHz}$, is 2.4 km; the height separation between the highest VHF echo and the highest UHF echo is $\sim 1.5\,\mathrm{km}$. Example II and the virtual radar of Fig. 31, example V, were chosen in order to shed some light on this experiment. It was somewhat surprising that the virtual radar of Fig. 17, representing the unfavourable polarization at matching height, gave a stronger power than the corresponding one of Fig. 31, from a cavitating state at the Airy maximum. Even so, we do not presently find a satisfactory agreement between observations and theoretical predictions. For example, the ion spectrum of Fig. 31 is rather strong, but the data of Djuth et al. (1994) do not show UHF ion spectra from the heights of the highest VHF spectra. Also, the value of E_0 in example V is too small relative to the value in example II, unless the absorption between is very large. It is not straightforward to explain these observations theoretically.

As noted in Sect. 4, in many experiments using the UHF radar, the "Kohl setup" (Sect. 4) was used, in order to obtain strong echoes (e.g. Kohl et al., 1987; Westman et al., 1995; Isham et al., 1999b). There is no published explanation presently of why this setup promotes detection of UHF spectra. In case these observations are cascades from the matching height, one possible explanation was discussed in Sect. 4, involving the reflected HF wave. It should be noted that if this is the explanation, the direction exactly along the magnetic field is not essential; even more favourable polarization can be obtained by pointing the radar at even larger angles to the vertical.

This explanation must assume that the anomalous absorption due to the intense Langmuir turbulence near the O-mode reflection height is not large. This, in turn, implies that the extremely large values of E_0 at Airy maximum, which were estimated in Sect. 4, must be assumed, and that the reflected wave contributes at VHF matching height. This, in turn, may not be consistent with cascading turbulence at VHF matching height.

In Isham et al. (1999b), EISCAT UHF observations implying cavitating Langmuir turbulence were claimed. In those experiments, the chirp technique (Birkmayer et al., 1986) was used. In chirped experiments, the frequency of the diagnostic radar pulse is varied linearly with time. The frequency shift of the natural plasma line satisfies the local Langmuir dispersion relation, and thus, a leading Taylor approximation will vary linearly with height locally. The radar frequency chirp is then tuned such that the natural plasma line backscatters in either the upshifted or downshifted band from a range of heights arrive at the receiver simultaneously at each frequency. In weak Langmuir turbulence theory, the excitations are also implied to satisfy the local Langmuir dispersion relation, so the radar backscatter from that should also contribute to this collected signal at the same frequency from a range of heights. In Birkmayer et al. (1986), it was discovered that in experiments at Arecibo, the HF-induced plasma line was displaced from this height-collected natural plasma line. One then had to conclude that the HF-induced excitation did not satisfy the Langmuir dispersion relation, and thus, had to be "strong" Langmuir turbulence, without having to be precise about the further meaning of that term. Equivalently, one could state that the backscatter came from density depletions at a larger height than the matching height, where the scattering excitations might satisfy the dispersion relation locally. The current picture of cavitating Langmuir turbulence can roughly be said to unify these two interpretations.

Isham et al. (1999b) report convincing results of this kind obtained using the EISCAT UHF radar. An outshifted feature ("OPL") coincides with the natural downshifted plasma line and thus, satisfies the dispersion relation. It is interpreted as corresponding to the "free mode" reported in Arecibo experiments. A $\sim 100\,\mathrm{kHz}$ broad feature starting at downshift near the applied frequency and moving inwards ("IPL", presumably corresponding to the "cavitation continuum" (DuBois et al., 2001)) does not. In this experiment, the radar was pointed along the magnetic field direction, 13° south (the "Kohl setup"). In this direction, the HF wave does not reach the critical level. Therefore, it is suggested in Isham et al. (1999b) that cavitation occurs at the height of the turning point. The studies at the end of Sect. 4, represented in Figs. 10–12, show that cavitation in the O-mode caustic region outside of the spitze is feasible; for example, the strength of the electric field could typically be a factor 2 stronger than at the VHF matching height. We have run numerically an example with nondimensional electric field strength $E_0 = 1.8$ and vertical polarization, $\Omega = 120$, and otherwise parameters as in example V. It went to cavitation; we show no further details since they are rather similar to example V.

Isham et al. (1999a) reported a variation in the height of the UHF ion line as a function of the radar line of sight, and compared it with the height of the VHF ion line at the vertical line of sight measured simultaneously. The UHF radar line

of sight was varied in steps from 0° to 13° south, and back, through several cycles. The UHF echoes occurred at heights up to about 5 km lower than the VHF echoes when the UHF radar pointed along the magnetic field, while the heights coincided when the UHF radar pointed vertically. In between, the height difference varied continuously and monotonically. The transmitted power in this experiment was of a similar order of magnitude as in other EISCAT experiments discussed here, such as Rietveld et al. (2000) and Isham et al. (1999b) (it was 160 MW ERP; the paper Isham et al., 1999a, contains a misprint; B. Isham, private communication).

Isham et al. (1999a) explained this along the same lines as the explanations in Isham et al. (1999b): that the echoes came from the caustic region, which, outside of the spitze, is at a lower height than the critical. However, according to the computations presented in Figs. 10 and 11 of the present paper, this appears unreasonable; in fact, for the data of Isham et al. (1999a) ($f_0 = 4.544\,\mathrm{MHz}$, $f_{ce} = 1.35\,\mathrm{MHz}$, $T_e = 1800°\,\mathrm{K}$), we have calculated that the O-mode turning point in the magnetic field direction ($1 - X = 0.0112$) is above the VHF vertical matching height ($1 - X = 0.0133$). The UHF matching height in the magnetic field direction is $1 - X = 0.153$, which with a scale height of 35 km, gives a height difference of 5.36 km. This is compatible with the height difference observed by Isham et al. (1999a) in the direction along the magnetic field. But in the other directions, the matching height should move even lower, due to the magnetic field term of Eq. (35). It is concluded that the observations of Isham et al. (1999a) of the continuous direction dependence of the locus of the UHF HF-induced ion line appear very difficult to incorporate into a consistent theoretical picture.

Altogether, a full quantitative agreement between published experimental work at Tromsø and the present model calculations cannot be reported. Future theoretical development, which at least might improve the agreement with the VHF results, should focus on the representation of the electron Landau damping in the model. There are at least three issues to consider: (i) for comparison with daytime experiments, it may influence predictions to include a population of photoelectrons in the representation of the Landau damping; (ii) the influence of the magnetic field on the Landau damping should be represented. This will introduce a potentially interesting dependence on the direction of $\boldsymbol{k}$; (iii) the development of the electron velocity distribution due to the turbulence could be incorporated, using a quasi-linear diffusion model, such as Sanbonmatsu et al. (1999, 2000). This may even allow for a higher value of the driving electric field near the reflection region, by damping the cavitating turbulence level. Altogether, such a development could improve the quantitative agreement between model predictions and experiments such as Rietveld et al. (2000) and Djuth et al. (2002).

Appendix A Numerical method

The time dependent, nonlinear, two-dimensional (in space), coupled set of partial differential Eqs. (6) is solved by a pseudospectral method (Canuto et al., 1988), i.e. the linear part of the spatial operators are computed in Fourier transform space, and the nonlinear parts are computed in real space, before transforming back to k-space. Thus, we propagate the Fourier coefficients $\Psi(k_{x,l}, k_{y,m}, t_n)$, $n(k_{x,l}, k_{y,m}, t_n)$, $\partial_t n(k_{x,l}, k_{y,m}, t_n)$ in time. The wave number mesh is defined by

$$k_{d,n} = (n - n_d/2)\Delta k_d \quad n \in [0, n_d - 1]\,, \tag{A1}$$

where $d = x, y$, $\Delta k_d = 2\pi/L_d$, where n_d is the number of mesh points along direction d, and L_d is the length of the periodic simulation cell in that direction. The discrete transform $\hat{f}$ of a function $f(x_l, y_m) = f_{l,m}$ sampled in the spatial mesh points

$$\begin{aligned}&(x_l, y_m) = (l * L_x/n_x, m * L_y/n_y),\\ &l \in [0, n_x - 1],\\ &m \in [0, n_y - 1]\end{aligned} \tag{A2}$$

is defined by

$$\begin{aligned}\hat{f}(k_{x,l}, k_{y,m}) &= \hat{f}_{l,m}\\ &= \sum_{j_1=0}^{n_x-1}\sum_{j_2=0}^{n_y-1} f_{j_1,j_2} \exp\left(\frac{-2i\pi j_1 l}{n_x}\right)\exp\left(\frac{-2i\pi j_2 m}{n_y}\right)\end{aligned} \tag{A3}$$

and the inverse transform is calculated in the same way, only with the opposite sign in the exponents and with the appropriate scaling $(1/(n_x n_y))$ for each coefficient. For the time propagation scheme, we use the second order method developed in Payne et al. (1983) for the ion-acoustic Eq. (6b) with the proper modification to be applicable for the two-dimensional case we study. For the first Zakharov Eq. (6a), we use a special time propagation scheme, where the linear part is solved exactly by noting that after we have discretized only in space and taken the spatial Fourier transform, Eq. (6a) can be written

$$d_t \hat{\Psi}_{\mathbf{k}} = \lambda_{\mathbf{k}} \hat{\Psi}_{\mathbf{k}} + \hat{G}_{\mathbf{k}}(\hat{\Psi}), \tag{A4}$$

where

$$\lambda_{\mathbf{k}} = -\nu_{\mathbf{k}} + i\left(\Omega - \Omega_B \frac{k_y^2}{k^2} - k^2\right) \tag{A5}$$

and

$$\hat{G}_{\mathbf{k}}(\hat{\Psi}) = -\frac{1}{k^2}\,\mathbf{k}\cdot[n(\mathbf{E} + \mathbf{E}_0)]_k\,, \tag{A6}$$

where now $\mathbf{E} = \nabla\Psi$. Equation (A4) can then be rewritten in the form

$$d_t(e^{-\lambda_{\mathbf{k}}}\hat{\Psi}_{\mathbf{k}}) = e^{-\lambda_{\mathbf{k}}}\hat{G}_{\mathbf{k}}(\hat{\Psi})\,. \tag{A7}$$

For $\mathbf{k} = \mathbf{0}$, we impose $n(\mathbf{k} = 0, t) = 0$ and $\Psi(\mathbf{k} = 0, t)$ constant. The linear part of this can now easily be solved

exactly, by integrating both sides from $n\delta t$ to $(n+1)\delta t$ to obtain

$$\hat{\Psi}_{\mathbf{k}}^{n+1} = e^{\lambda_{\mathbf{k}} t}\hat{\Psi}_{\mathbf{k}}^{n} + e^{\lambda_{\mathbf{k}} t}\int_{n\delta t}^{(n+1)\delta t} e^{-\lambda_{\mathbf{k}} t'}\hat{G}_{\mathbf{k}}(\hat{\Psi})dt'. \qquad \text{(A8)}$$

This way of treating the linear part is both unconditionally stable and exact, and the accuracy and stability restrictions of the time propagation method arise solely from the nonlinear part (Canuto et al., 1988). For the nonlinear part (the integral part of equation (A8)), we may use any well suited approximative method for the integral. We have chosen to use a second order explicit method (Adams Bashforth) (Burden and Faires, 1989). This method is accurate and fast, in that we only have to compute the spatial operators once every elementary time step. In order to ensure stability of the numerical scheme, we typically have to use an elementary time step δt in the range 10^{-3}–10^{-4}, depending on the width of the resulting modal spectra. In cases of cavitation, even smaller values had to be used.

For every numerical solution we present, the initial condition (at $t = 0$) of Ψ, n and $\partial_t n$ is given as white noise, i.e. each Fourier coefficient of these quantities are set to $\sim A\exp(i2\pi\phi)$, where A is typically 10^{-1} and ϕ is determined by a random number generator in the interval $[0, 1)$. Numerical experiments show that the particular choice of initial conditions does not affect the saturated state, and all of the spectra presented here are based on results obtained after the initial transient phase of the development of the Langmuir turbulence is over.

Acknowledgements. E.H. was a guest at Los Alamos National Laboratory (LANL), theoretical division, during fall 1994 and spring 1995, at an early stage of this work. The work continued during E.M.'s stay at LANL, hosted by Center for Nonlinear Studies, and Theoretical Division, during October-December 1998. E.H. was supported by the Research Council of Norway (NFR) under project 100574/410 during 1993–1996. The work has received support from the Norwegian Super-Computing Committee through a grant of computing time. The numerical data of Figs. 13–31 have been obtained using the computers Victorio and Nana at the High Performance Computing Center (HPC) at University of Tromsø. E.M. and E.H. are grateful for all helpful assistance from the staff at HPC, in particular Roy Dragseth. E.M. thanks Frank Djuth, Mike Rietveld, Brett Isham, Tor Hagfors, and Cesar La Hoz for helpful discussions.

References

Abramowitz, M. and Stegun, I. A.: Handbook of Mathematical Functions, Dover Publications, 1970.

Birkmayer, W., Hagfors, T., and Kofman, W.: Small-scale plasma density depletions in Arecibo high-frequency modification experiments, Phys. Rev. Lett., 57, 1008–1011, 1986.

Budden, K. G. The Propagation of Radio Waves, Cambridge University Press, New York, 1985.

Burden, R. L. and Faires, J. D.: Numerical Analysis, PWS-Kent Publishing Company, 1989.

Canuto, C., Hussaini, M. Y., Quarterino, A., and Zang, T. A.: Spectral Methods in Fluid Dynamics, vol. 16 of Springer Ser. in Comput. Phys., Springer-Verlag, New York, 1988.

Carlson, H. C., Gordon, W. E., and Showen, R. L.: High-frequency induced enhancements of the incoherent scatter spectrum at Arecibo, J. Geophys. Res., 77A, 1242–1250, 1972.

Cheung, P., DuBois, D. F., Fukuchi, T., Kawan, K., Rose, H. A., Russell, D., Tanikawa, T., and Wong, A. Y.: Investigation of strong Langmuir turbulence in ionospheric modification, J. Geophys. Res., 97A, 10 575–10 600, 1992.

Cheung, P. Y., Sulzer, M. P., DuBois, D. F., and Russel, D. A.: High power HF-induced Langmuir turbulence in the smooth ionosphere at Arecibo: Ii. low duty cycle, altitude resolved, observations at Arecibo, Phys. Plasmas, 8, 802–812, 2001.

Cheung, P. Y., Wong, A. Y., Tanikawa, T., Santoru, J., DuBois, H. A., Rose, D. F., and Russell, D.: Short time scale evidence for strong Langmuir turbulence during HF heating of the ionosphere, Phys. Rev. Lett., 62, 2676–2679, 1989.

Das, A. C., Fejer, J. A., and Martinic, N. J.: Three-dimensional saturation spectrum of the parametric decay instability, Radio Sci., 20, 813–818, 1985.

Djuth, F. T., Isham, B., Rietveld, M. T., Elder, J. H., Hagfors, T., and La Hoz, C.: The first one hundred milliseconds of HF modification at Tromsø, Norway, submitted to J. Geophys. Res., 2002.

Djuth, F. T., Stubbe, P., Sulzer, M. P., Kohl, H., Rietveld, M. T., and Elder, J. H.: Altitude characteristics of plasma turbulence excited with the Tromsø superheater, J. Geophys. Res., 99A, 333–339, 1994.

Djuth, F. T., Sulzer, M. P., and Elder, J. H.: High resolution observation of HF-induced plasma waves in the ionosphere, Geophys. Res. Lett., 17, 1893–1896, 1990.

Doolen, G. D., DuBois, D. F., and Rose, H. A.: Nucleation of cavitons in strong Langmuir turbulence, Phys. Rev. Lett., 54, 804–807, 1985.

DuBois, D. F., Hanssen, A., and Rose, H. A., Comment on "Langmuir turbulence and ionospheric modification" by P. Stubbe, H. Kohl and M. T. Rietveld, J. Geophys. Res., 97A, 15 059–15 065, 1992.

DuBois, D. F., Hanssen, A., Rose, H. A., and Russell, D.: Excitation of strong Langmuir turbulence in the ionosphere: Comparison of theory and observations, Phys. Fluids, B5, 2616–2622, 1993a.

DuBois, D. F., Hanssen, A., Rose, H. A., and Russell, D.: Space and time distribution of HF excited Langmuir turbulence in the ionosphere: Comparison of theory and experiment, J. Geophys. Res., 98A, 17 543–17 567, 1993b.

DuBois, D. F., Rose, H. A., and Russell, D.: Power spectra of fluctuations in strong Langmuir turbulence, Phys. Rev. Lett., 61, 2209–2212, 1988.

DuBois, D. F., Rose, H. A., and Russell, D.: Excitation of strong Langmuir turbulence in plasmas near critical density: Application to HF heating of the ionosphere, J. Geophys. Res., 95A, 21 221–21 272, 1990.

DuBois, D. F., Rose, H. A., and Russell, D.: Coexistence of parametric decay cascades and caviton collapse at subcritical densities, Phys. Rev. Lett., 66, 1970–1973, 1991.

DuBois, D. F., Rose, H. A., and Russell, D.: Saturation of radiation-induced parametric instabilities by excitation of Langmuir turbulence, Physica Scripta, T63, 16– 27, 1996.

DuBois, D. F., Russell, D. A., Cheung, P. Y., and Sulzer, M. P.: High power HF-induced Langmuir turbulence in the smooth ionosphere at Arecibo: I. theoretical preductions for altitude resolved plasma line radar spectra, Phys. Plasmas, 8, 791–801, 2001.

DuBois, D. F., Russell, D., and Rose, H. A.: Reduced description of strong Langmuir turbulence from kinetic theory, Phys. Plasmas, 2, 76–96, 1995.

Dyachenko, A. I., Pushkarev, A. N., Rubenchik, A. M., Sagdeev, E. Z., Shvets, V. F., and Zakharov, V. E.: Computer simulation of Langmuir collapse, Physica, D52, 78–102, 1991.

Fejer, J. A. and Kopka, H.: The effect of plasma instabilities on the ionospherically reflected wave from a high-power transmitter, J. Geophys. Res., 86A, 5746–5750, 1981.

Fejer, J. A. and Kuo, Y.-Y.: Structure in the nonlinear saturation spectrum of parametric instabilities, Phys. Fluids, 16, 1490–1496, 1973.

Fejer, J. A., Sulzer, M. P., and Djuth, F. T.: Height dependence of the observed spectrum of radar backscatter from HF-induced ionospheric Langmuir turbulence, J. Geophys. Res., 96A, 15 985–16 008, 1991.

Forme, F.: Parametric decay of beam-driven Langmuir wave and enhanced ion-acoustic fluctuations in the ionosphere: a weak turbulence approach, Ann. Geophysicae, 17, 1172–1181, 1999.

Frolov, V. L., Komrakov, G. P., Sergeev, E. N., Thidé, B., Waldenvik, M., and Veszelei, E.: Results of the experimental study of narrow continuum features in stimulated ionospheric emission spectra, Izv. Vys. Uch. Zav. Radiofiz., 40, 1091–1112, 1997 (Engl. transl. Radiophys. Quant. Electron., 40, 731–744, 1997).

Gurevich, A. V., Dimant, Y. S., Milikh, G. M., and Vas'kov, V. V.: Multiple acceleration of electrons in the regions of high-power radio wave reflection on the ionosphere, J. Atmos. Terr., Phys., 47, 1057–1070, 1985.

Hagfors, T., Kofman, W., Kopka, H., Stubbe, P., and Aijanen, T.: Observations of enhanced plasma lines by EISCAT during heating experiments, Radio Sci., 18, 861–866, 1983.

Hammet, G. W. and Perkins, F. W.: Fluid moment models for Landau damping with applications to the ion-temperature-gradient instability, Phys. Rev. Lett., 64, 3019–3022, 1990.

Hanssen, A.: Electromagnetically driven Langmuir turbulence in the ionosphere, Ph.D. dissertation, Univ. of Tromsø, Norway, 1992.

Hanssen, A., Mjølhus, E., DuBois, D. F., and Rose, H. A.: Numerical test of the weak turbulence approximation to ionospheric Langmuir turbulence, J. Geophys. Res., 97A, 12 073–12 091, 1992.

Helmersen, E. and Mjølhus, E.: A semikinetic model for ionospheric Langmuir turbulence, J. Geophys. Res., 99A, 17 623–17 629, 1994.

Isham, B., La Hoz, C., Rietveld, M. T., Hagfors, T., and Leyser, T. B.: Cavitating Langmuir turbulence observed during high-latitude ionospheric wave interaction experiments, Phys. Rev. Lett., 83, 2576–2579, 1999b.

Isham, B., Rietveld, M. T., Hagfors, T., La Hoz, C., Mishin, E., Kofman, W., Leyser, T. B., and van Eyken, A. P.: Aspect angle dependence of HF enhanced incoherent backscatter, Adv. Space Res., 24, 1003–1006, 1999a.

Jones, T. B., Robinson, T., Stubbe, P., and Kopka, H.: Frequency dependence of anomalous absorption caused by high power waves, J. Atmos. Terr. Phys., 46, 147–150, 1984.

Kohl, H. and Rietveld, M. T.: Harmonics of the ion acoustic frequency in the heater induced ion spectrum, J. Geophys. Res., 101, 5391–5395, 1996.

Kohl, H., Kopka, H., La Hoz, C., and Stubbe, P.: Propagation of artificially excited Langmuir waves in the ionosphere, Radio Sci., 22, 655–661, 1987.

Kohl, H., Kopka, H., Stubbe, P., and Rietveld, M. T.: Introduction to ionospheric heating experiments at Tromsø –II. Scientific problems, J. Atmos. Terr. Phys., 55, 601–613, 1993.

Krasnoselskikh, V. V. and Sotnikov, V. I.: Plasma wave collapse in a magnetic field, Fiz. Plasmy, 3, 872–879, 1977 (Engl. transl. Sov. J. Plasma Phys., 3, 491–495, 1977).

Lundborg, B. and Thidé, B.: Standing wave pattern of HF radio waves in the ionospheric reflection region, 1. applications, Radio Sci., 21, 486–500, 1986.

Mjølhus, E.: On linear conversion in a magnetized plasma, Radio Sci., 25, 1321–1339, 1990.

Mjølhus, E., Hanssen, A., and DuBois, D. F.: Radiation from electromagnetically driven Langmuir turbulence, J. Geophys. Res., 100A, 17 527–17 541, 1995.

Mjølhus, E., Helmersen, E., and DuBois, D. F., Significance of short-scale irregularities for radar diagnostics of HF driven Langmuir turbulence in the ionosphere, J. Geophys. Res., 2001, in print.

Nicholson, D. R., Payne, G. L., Downie, R. M., and Sheerin, J. P.: Solitons versus parametric instabilities during ionospheric heating, Phys. Lett., 52, 2152–2155, 1984.

Payne, G. L., Nicholson, D. R., and Downie, R. M.: Numerical solution of the Zakharov equations, J. Comput. Phys., 50, 482–498, 1983.

Perkins, F. W., Oberman, C., and Valeo, E. J.: Parametric instabilities and ionospheric modifications, J. Geophys. Res., 79A, 1478–1496, 1974.

Petviashvili, V. I., Three-dimensional solitons of extraordinary and plasma waves, Fiz. Plasmy, 1, 28–31, 1975 (Engl. transl. Sov. J. Plasma Phys., 1, 15–16, 1975).

Rietveld, M. T., Isham, B., Kohl, H., La Hoz, C., and Hagfors, T.: Measurements of HF-enhanced plasma and ion lines at EISCAT with high altitude resolution, J. Geophys. Res., 105A, 7429–7439, 2000.

Robinson, P. A., Newman, D. L., and Goldman, M. V.: Three-dimensional strong Langmuir turbulence and wave collapse, Phys. Rev. Lett., 61, 702–705, 1988.

Rypdal, K. and Cragin, B.: HF-induced parametric decay in presence of field-aligned irregularities, J. Geophys. Res., 84A, 6407–6416, 1979.

Sanbonmatsu, K. Y., Vu, H. X., DuBois, D. F., and Bezzerides, B.: A new paradigm for the self-consistent modelling of wave-particle and wave-wave interactions in the saturation of electromagnetically driven parametric instabilities, Phys. Rev. Lett., 82, 932–935, 1999.

Sanbonmatsu, K. Y., Vu, H. X., DuBois, D. F., and Bezzerides, B.: Quantitative comparison of reduced-description particle-in-cell and quasilinear-Zakharov models for parametrically excited Langmuir turbulence, Phys. Plasmas, 7, 2824–2841, 2000.

Shapiro, V. D. and Shevchenko, V. I.: Strong turbulence of plasma oscillations, Handbook of Plasma Physics, Elsevier, New York, (Eds) Galeev, A. A. and Sudan, R. N., p. 123, 1984.

Sprague, R. A. and Fejer, J. A.: Simultaneous excitation of parametric decay cascades and of the OTSI in 1D numerical simulations based on Zakharov's equations, J. Geophys., Res., 100A, 23 959–23 972, 1995.

Stix, T. H.: The theory of plasma waves, McGraw-Hill, New York, 1962.

Stubbe, P., Kohl, H., and Rietveld, M. T.: Langmuir turbulence and ionospheric modification, J. Geophys. Res., 97A, 6285–6297, 1992a.

Stubbe, P., Kohl, H., and Rietveld, M. T.: Reply, J. Geophys. Res., 97, 15 067–15 071, 1992b.

Stubbe, P., Kopka, H., Rietveld, M. T., Frey, A., Hoegh, P., Kohl, H., Nielsen, E., Rose, G., La Hoz, C., Barr, R., Derblom, H., Hedberg, Å., Thidé, B., Jones, T. B., Robinson, T., Brekke, A.,

Hansen, T., and Holt, O.: Ionospheric modification experiments with the Tromsø heating facility, J. Atmos. Terr. Phys., 47, 1151–1163, 1985.

Sulzer, M. P. and Fejer, J. A.: Radar spectral observations of HF-induced ionospheric Langmuir turbulence with improved range and time resolution, J. Geophys. Res., 99A, 15 035–15 050, 1994.

Wang, J. G., Payne, G. L., DuBois, D. F., and Rose, H. A.: One-dimensional simulations of Langmuir collapse in a radiation-driven plasma, Phys. Plasmas, 1, 2531–2546, 1994.

Wang, J. G., Payne, G. L., DuBois, D. F., and Rose, H. A.: Vlasov simulation of modulational instability and Langmuir collapse, Phys. Plasmas, 2, 1129–1139, 1995.

Westman, A., Leyser, T. B., Wannberg, G., and Rietveld, M. T.: Tristatic EISCAT-UHF measurements of the HF modified ionosphere for low background electron temperatures, J. Geophys. Res., 100A, 9717–9728, 1995.

Wong, A. Y. and Taylor, R. J.: Parametric excitation in the ionosphere, Phys. Rev. Lett., 27, 644–647, 1971.

Zakharov, V. E.: Collapse of Langmuir waves, Sov. Phys. JETP, Engl. Transl., 35(5), 908–914, 1972.